TEKTONIKA

3D Interaction of Tectonics and Surface Processes Explains Fault Network Evolution of the Dead Sea Fault

Esther L. Heckenbach [1,2], Sascha Brune [*1,2], Anne C. Glerum [1], Roi Granot [3], Yariv Hamiel [4], Stephan V. Sobolev [1,2], Derek Neuharth [1,5]

[1]Helmholtz Zentrum Potsdam - Deutsches GeoForschungsZentrum GFZ, Potsdam, Germany | [2]University of Potsdam - Institute of Geosciences, Potsdam, Germany | [3]Ben-Gurion University of the Negev, Beer-Sheva, Israel | [4]Geological Survey of Israel, Jerusalem, Israel | [5]ETH Zürich, Zürich, Switzerland

Abstract Releasing and restraining bends are complementary features of continental strike-slip faults. The Dead Sea Basin of the strike-slip Dead Sea Fault is a classical example of a releasing bend with an asymmetric, deep basin structure. However, the intrinsic relationship to its northern counterpart, the restraining bend that created the Lebanese mountains, remains unclear. Here, we present 3D coupled geodynamic and landscape evolution models that include both the releasing and the restraining bend in a single framework. These simulations demonstrate that the structural basin asymmetry is a consequence of strain localization processes, while sediments control the basin depth. Local extension emerges due to strength heterogeneities and a misalignment of faults and the overall stress field in an area where regional tectonics are dominated by strike-slip motion. Furthermore, we reveal a crustal thinning and thickening pattern that intensifies with surface process efficiency. Along-strike deformation is linked through coupled crustal flow driven by gravitational potential energy which is opposed by deposition at the releasing bend and enhanced by erosion around the restraining bend. With much of our model setup being kept generic, our results provide templates for the evolution of fault bends worldwide.

Executive Editor:
Craig Magee
Associate Editor:
Guillaume Duclaux
Technical Editor:
Mohamed Gouiza

Reviewers:
Attila Balazs
Joao Duarte

Submitted:
20 December 2023
Accepted:
23 May 2024
Published:
20 August 2024

1 Introduction

Continental transform faults are highly localized strike-slip zones that accumulate tens to hundreds of kilometers of shear motion (*Norris and Toy*, 2014). They often form as a network of fault segments with clearly visible fault traces. Besides the Dead Sea Fault (*Dubertret*, 1932), other prominent examples of continental transform faults are the San Andreas Fault of California (*Lawson*, 1895; *Gilbert et al.*, 1907), the East and the North Anatolian Fault in Turkey (*Ketin*, 1948; *Arpat*, 1972; *Seymen and Aydin*, 2023), the Alpine Fault of New Zealand (*Wellman*, 1952), and the Altyn Tagh Fault in Tibet (*Tapponnier and Molnar*, 1977).

While transform fault systems are primarily associated with strike-slip motion, stepovers and fault segmentation result in regional transpressional regimes at restraining bends and transtensional regimes at releasing bends (*Crowell*, 1974; *Mann*, 2007). Fault bends are responsible for distinct topographical features, including the formation of push-up mountains at restraining bends and deep pull-apart basins at releasing bends. Notably, the Dead Sea pull-apart basin has the world's lowest on-land elevation with 430 m below global sea level.

The Dead Sea Fault (DSF) system (Figure 1a) formed less than 20 Myr ago (Ma) during the fragmentation of the northeastern Nubian Plate into the Arabian and Sinai Plates (*Garfunkel*, 1981). It is embedded in a complex tectonic framework connecting the Red Sea rift in the south to the Bitlis-Zagros mountain range in the north (*Quennell*, 1959; *DESERT Group et al.*, 2004). The southern part of the DSF accommodates several narrow pull-apart basins resulting from releasing bends with thick sedimentary infill (*Garfunkel and Ben-Avraham*, 2001) contrasting the high elevations of the Lebanese mountains within the restraining bend in the north. The central topographic depression that divides the Lebanese mountains (the Beqaa valley) is situated in a region characterized by inherited structures (e.g. *Gomez et al.*, 2007; *Fedorik et al.*, 2022) and is believed to have originated as a syncline (*Lateef*, 2007, and references therein).

The DSF system has been intensively studied through various geophysical methods (Figure 1). Major earthquakes are concentrated on the faults along the strike-slip and releasing bend sections,

*✉ sascha.brune@gfz-potsdam.de

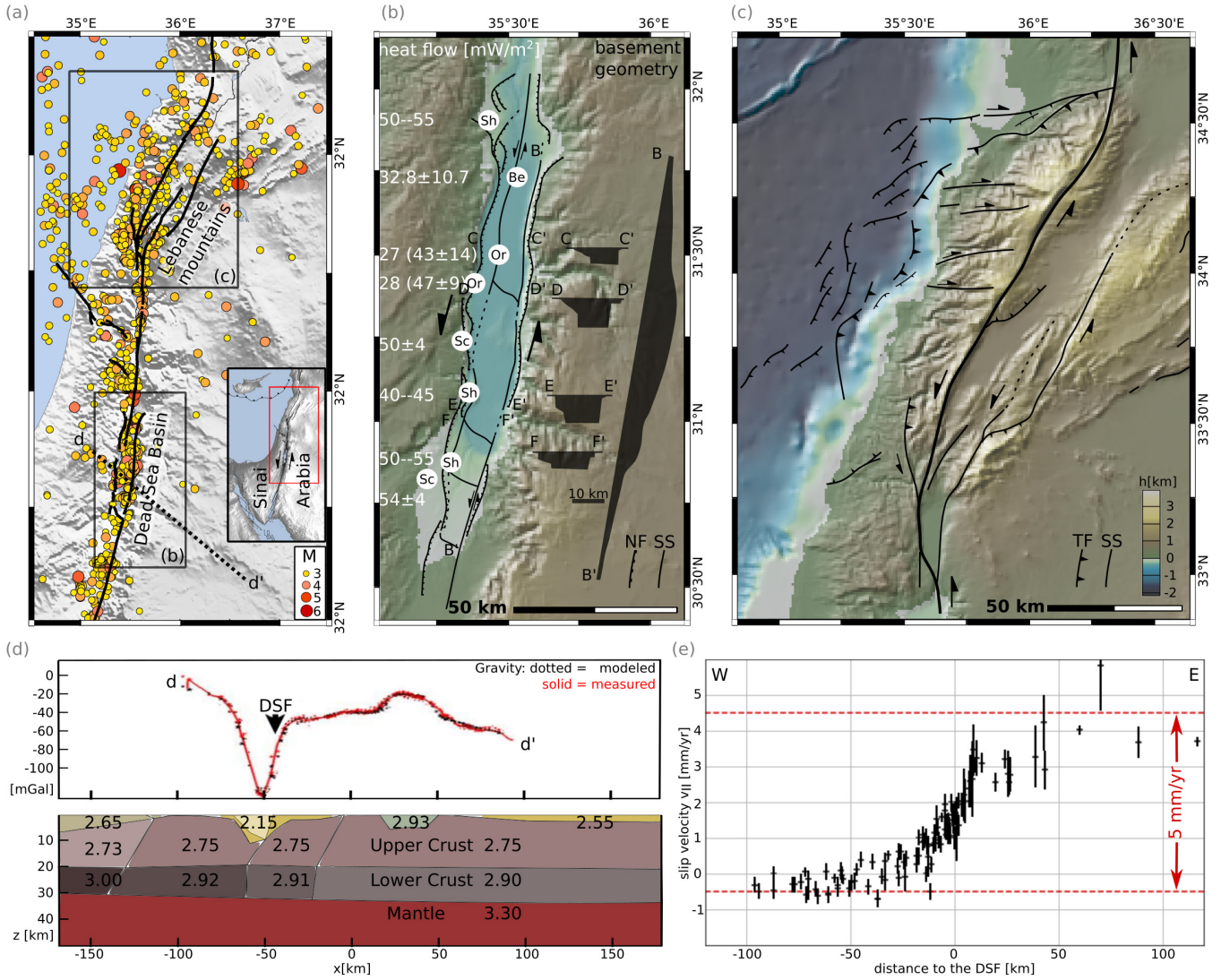

Figure 1 – A summary of the available geophysical data along the Dead Sea Fault (DSF). **(a)** Topographic relief map (ETOPO 2022, https://doi.org/10.25921/fd45-gt74) with locations and magnitudes of recorded seismicity since 1985 according to the GSI seismic catalogue (eq.gsi.gov.il/en/earthquake/searchEQS.php) and main surface outlines of the DSF system (*Hamiel and Piatibratova*, 2021). **(b)** Topographic relief map of the Dead Sea Basin with the fault network outlined in black after Figure 1 in *Smit et al.* (2008) and the cross-sectional basement geometry in black after Figure 7 in *Ten Brink et al.* (1993). White circles and corresponding values indicate surface heat flow measurements obtained within the basin. Values belonging to locations marked as Sh (*Shalev et al.*, 2013) indicate the range of values associated with the color of their map at this point. The mean of several measurement points is provided by Be (*Ben-Avraham et al.*, 1978), while Or (*Oryan et al.*, 2019) values show their measurement and the correction range in brackets and Sc (*Schütz et al.*, 2014) provide an uncertainty range. **(c)** Topographic relief map of the Lebanese restraining bend with the fault network outlined after Figure 1 in *Elias et al.* (2007), and modified according to *Hamiel and Piatibratova* (2021). Topography of both (b) and (c) has been plotted using GeoMapApp with the same color scale as shown in (c) (geomapapp.org, *Ryan et al.*, 2009). See rectangles in (a) for locations of (b) and (c). **(d)** Gravity profile and crustal density [Mg/m^3] model modified from Figure 5 in *Götze et al.* (2007). The location of profile d–d' is shown in (a). **(e)** Fault-parallel velocities as a function of distance from the fault obtained from GPS data of selected stations between 30°N and 32.3°N (*Hamiel and Piatibratova*, 2021, Figure 2, profiles B–E) representing strike-slip and transtensional deformation regimes in the area. Velocity is shown relative to the Sinai Plate (see inset in (a)).

whereas the fault network is more complex and seismicity more wide-spread at the restraining bend (*Elias et al.*, 2007; *Smit et al.*, 2008; *Wetzler and Kurzon*, 2016).

Gravity measurements show that the DSF is located where the 35 km thick continental crust of the Arabian Plate thins towards the Sinai Plate and the Mediterranean Sea (*Götze et al.*, 2007) (Figure 1d). Today, the Dead Sea Basin (DSB) is characterized by a prominent and well-defined gravitational low between these two plates (Figure 1d) and exhibits intriguingly small surface heat flow, which can be as low as 27–40 mW/m^2 (Figure 1b in white) (*Ben-Avraham et al.*, 1978; *Shalev et al.*, 2013; *Schütz et al.*, 2014; *Oryan et al.*, 2019). These values are, however, debated as they are in strong contrast to the surface heat flow values of 50–60 mW/m^2 seen farther from the basin (*Förster et al.*, 2010; *Shalev et al.*, 2013).

Seismic data suggest that the sedimentary infill is

8–12 km thick, which makes the basin roughly as deep as it is wide (*Ten Brink et al.*, 1993) (Figure 1b). These data furthermore reveal that the sediment infill and basement topography feature a distinct asymmetry involving a steeply sloping eastern side and a gentler sloping western side. Together with this asymmetry, the steep basin-ward dipping strike-slip border faults led previous studies to suggest and explore an extensional component across the basin and the transform sections of the DSF (*Quennell*, 1959; *Garfunkel*, 1981; *Ben-Avraham and Zoback*, 1992; *DESERT Group et al.*, 2004; *Sobolev et al.*, 2005; *Petrunin and Sobolev*, 2006; *Smit et al.*, 2008, 2010; *Petrunin et al.*, 2012).

Far-field extension has been attributed to a shift in plate kinematics due to changes in the direction and velocity of the Red Sea opening around ∼10–5 Ma (e.g. *Garfunkel*, 1981; *Joffe and Garfunkel*, 1987; *Smit et al.*, 2010; *Reilinger and McClusky*, 2011). However, inversions of regional GPS data do not disclose a present-day component of far-field extension (*Le Beon et al.*, 2008; *Hamiel and Piatibratova*, 2021). Instead, these demonstrated that local extension is confined to areas where faults deviate from the along-strike DSF direction within releasing bends.

The origin of the low surface heat flow, the elongated basin geometry and whether temporal changes in plate kinematics shaped the observed asymmetry are among the major ongoing discussion points concerning the area.

In previous modeling studies, restraining and releasing bends such as found in the DSF system have primarily been investigated separately, which entails that possible interactions during their evolution have been neglected.

These studies underlined the crucial role of a thick ductile layer (*Petrunin and Sobolev*, 2006; *Smit et al.*, 2008) that decouples the brittle crust and upper mantle in the formation of narrow pull-apart basins. Additionally, they highlighted the significance of the development of an isolated crustal block for very thick sedimentary infill and low surface heat flow values (*Ben-Avraham and Schubert*, 2006; *Ben-Avraham et al.*, 2010). For restraining bends, previous studies have demonstrated that block rotation takes place prior to strain partitioning, as evidenced by paleomagnetic rotations, as well as by the present-day orientation of rivers and earthquake focal mechanisms (*Gomez et al.*, 2007; *Goren et al.*, 2015; *Dembo et al.*, 2021). Throughout this study, strain partitioning refers to the process where initially a single fault accommodates the full oblique motion, but experiences differentiation with ongoing tectonic deformation such that in the end one set of faults hosts pure strike-slip motion and another set hosts pure dip-slip motion.

In this study, we utilize geodynamic models to investigate the evolution of strike-slip faults that include both a releasing and a restraining bend in a periodic setup. Compared to previous studies featuring only one kind of bend, this has the advantage that possible interactions are included and fault kinematics do not need to be prescribed in the boundary conditions but can evolve according to the accumulation of stress and strain. Our target region is the Dead Sea Fault, but the models are kept generic to a great extent. The results are hence transferable to other fault bends worldwide. First, we describe the mechanisms that control the evolution of the model pull-apart basin and compare it to observations from the DSB. We show that asymmetry and local extension along a modeled transform fault can result from strength heterogeneities without requiring far-field divergence. Additionally, we investigate how sediment deposition changes the longevity of the pull-apart basin. Finally, we present new insights into feedbacks between tectonics and surface processes and find that erosion and sedimentation can provide a long-distance connection between a releasing and restraining bend at crustal scale.

2 Methods

2.1 ASPECT and FastScape

Computations were performed with the geodynamic finite element software ASPECT (Advanced Solver for Planetary Evolution, Convection, and Tectonics, aspect.geodynamics.org, see *Kronbichler et al.*, 2012; *Heister et al.*, 2017; *Gassmöller et al.*, 2018).

We employ ASPECT to solve for the governing equations describing the conservation of mass, momentum, and energy. We use an extended Boussinesq approximation with an infinite Prandtl number (see Supplementary Material, eq. 1–8). The classical Boussinesq approximation implies incompressibility of the involved materials (*Rayleigh*, 1916) allowing for a more efficient modeling strategy. In this case it is assumed that density variations are small enough that they can be neglected everywhere except for buoyancy (right-hand-side term in Eq. S1). The extended Boussinesq approximation additionally includes the processes of adiabatic heating and shear heating when computing the temperature evolution (the two right-most terms in Eq. S3), but neglects the associated volume and density changes (*van Zelst et al.*, 2022). We employ this approximation here as it is well justified in models of lithosphere deformation where the relatively shallow modeling domain implies only minor adiabatic temperature changes. A high Prandtl number indicates that momentum transport and with it convection dominates over heat diffusion, which means that the temperature distribution has an important effect on the viscosity of the modeled rocks. Assuming an infinite Prandtl number means that the viscous resistance to inertia is so high that inertia can be ignored in the governing equations.

For each material (e.g., upper crust) and plastic strain, an additional advection equation is solved

(continuous field method). Nonlinearities in the rheology (*Glerum et al.*, 2018) are iterated out using a Newton solver scheme (*Fraters et al.*, 2019). A Newton solver is a powerful tool used in solving mathematical equations that depend on their own solutions, for example when the viscosity depends on the strain rate and pressure. This approach starts with an initial guess of the solution and then refines it through a series of calculations until a solution is found that meets a certain level of accuracy (tolerance).

Furthermore, we employ the recently established two-way coupling between ASPECT and the surface-processes software FastScape (fastscape.org, *Braun and Willett*, 2013; *Yuan et al.*, 2019a,b). The coupling is illustrated in Figure 2 and works as follows (*Neuharth et al.*, 2022a,b): at the beginning of each geodynamic time step, ASPECT hands over the vertical and horizontal surface velocity to FastScape for use in uplift and horizontal advection, respectively. Then, equations describing river incision (extended stream power law), hillslope diffusion and marine sediment transport are solved. The intensity of their combined effect is described as surface process efficiency throughout this study. All sediments in the basin derive from the model domain and we do not include additional sources like pelagic sedimentation. After a prescribed number of FastScape time steps, the updated surface topography is given back to ASPECT. ASPECT's mesh is then modified by computing the velocity of the mesh surface such that it captures the update in topography over the current timestep. To avoid distorted cells, the velocity of the mesh interior is distributed smoothly across the model domain by solving a Laplace equation (see *Rose et al.*, 2017). Subsequently, ASPECT solves the governing equations.

FastScape uses the user-set sea level as the reference height for all erosional processes such that after an infinite amount of time, FastScape's set of equations would level all non-marine topography to this height in the absence of tectonic uplift. However, to account for the smaller water bodies that often form at releasing bends in general, and in particular because the surface of the Dead Sea is below global sea level, we need to discriminate between local and global sea level and their effect on fluvial erosion. We therefore introduce a new parameter, the regional erosional base level, in the ASPECT-FastScape coupling. The new parameter minimizes mass loss and assures that only a small lacustrine area at the releasing bend evolves, while the surroundings remain as elevated topography. The specific version of ASPECT and FastScape used in this paper can be found at zenodo.org/doi/10.5281/zenodo.10405076 (*Heckenbach*, 2023).

2.2 Model Setup

We conducted a series of 3D box simulations to investigate the influence of boundary and initial conditions, as well as different surface process efficiencies, on the evolution of a generic strike-slip setup comprising two stepovers that evolve into a restraining and a releasing bend (Figure 2). Model parameters are shown in the supplementary Tables S1 and S2. All ASPECT and FastScape parameter values can be found in the ASPECT input files provided at zenodo.org/doi/10.5281/zenodo.10405076.

2.2.1 Geometry and Resolution

The geodynamic model domain is 600 km long (x-direction), 152 km wide (y-direction) and 100 km deep (z-direction). We use mesh refinement such that the uppermost 15 km and a box of 45 km depth and 36 km width along the fault have a resolution of 1 km, while resolution gradually decreases to 4 km at the bottom of the domain. The mesh of the FastScape 2D domain that spans the top surface of the 3D ASPECT model has a resolution of 500 m. The local FastScape sea level that determines sediment accommodation space is set to be 500 m lower than the regional erosional base level, as the former represents the Dead Sea or similar water-filled pull-apart basins, while the latter represents global sea level.

2.2.2 Initial Conditions

The initial model setup consists of five initially horizontal geologic units: a sedimentary cover (top nodes only) on top of a 20 km thick upper and a 13 km thick lower crust that are underlain by 67 km of lithospheric mantle and a thin layer of asthenosphere (Figure 2a). The asthenosphere only covers the bottom nodes, but increases in volume where the lithosphere is thinned. Initial reference crustal layer thicknesses and all densities are chosen according to the eastern part of the gravity profile crossing the DSF (*Götze et al.*, 2007) (see Supplementary Table S1 for all material properties).

It should be noted that these published densities are in-situ densities based on seismic velocities from the DESERT seismic line (*DESERT Group et al.*, 2004), while the geodynamic models require reference densities as an input for the temperature-dependent density. In our models, the reference densities were chosen such that values at the center of each layer match the in-situ densities inferred from geophysical data (see values in Figure 2a). The chosen model lithosphere of 100 km is slightly thicker than the current lithosphere along the DSF (*Mohsen et al.*, 2011) to preserve the generic character of the models. This thickness, however, coincides with the lithosphere structure at the onset of DSF formation, prior to a hypothesized delamination event (*Petrunin et al.*, 2012).

The initial temperature distribution is based on a steady-state 1D conductive continental geotherm in the lithosphere and on an adiabat below the lithosphere (see Figure 2c and Supplementary Table S1). The top surface is fixed to 273 K and the

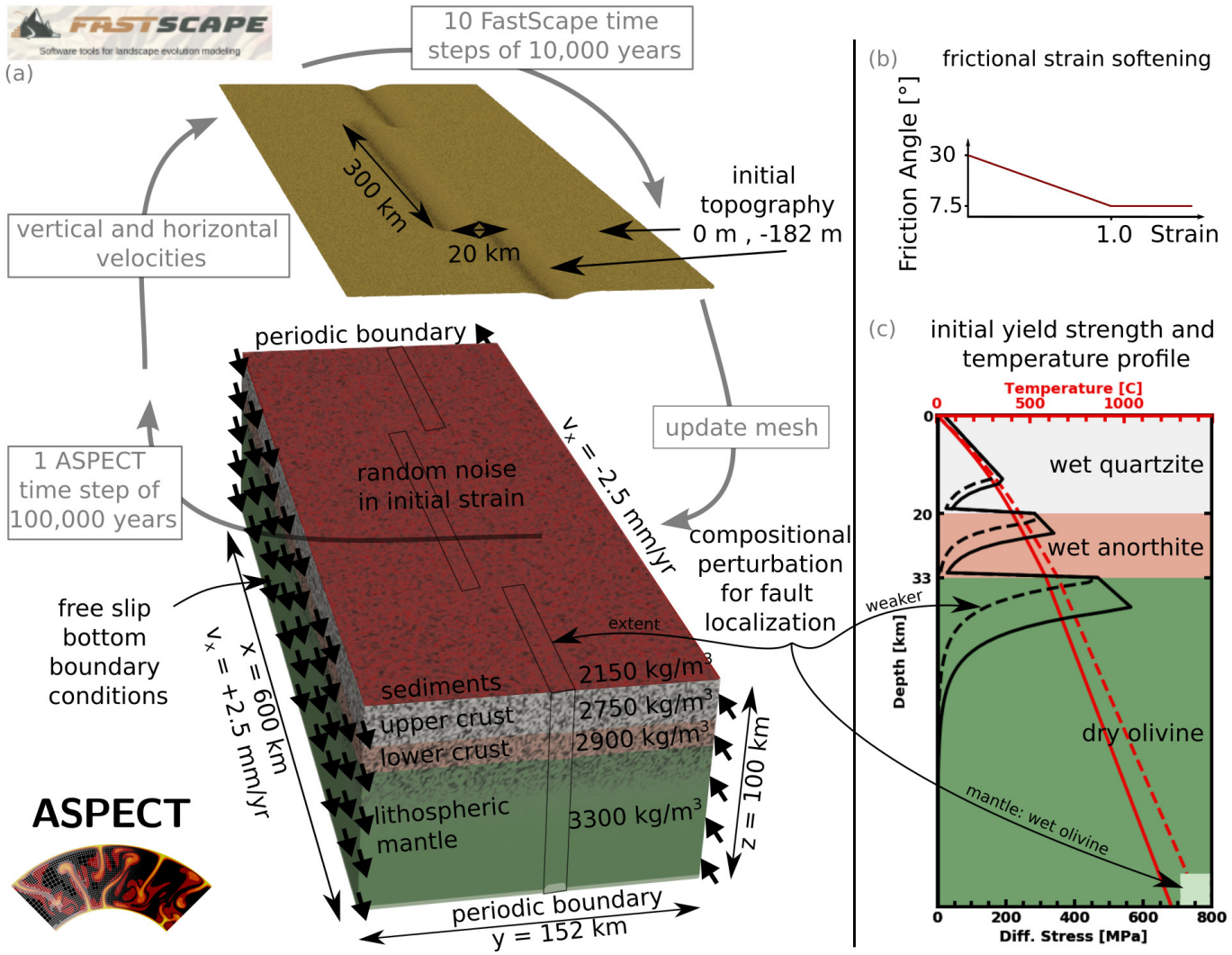

Figure 2 – **(a)** Initial and boundary conditions of the reference model using the two-way coupled ASPECT-FastScape software. Rheological parameters showing **(b)** weakening of the internal angle of friction with accumulated plastic strain and **(c)** temperature and strength profiles for a representative strain rate of $1{\cdot}10^{-15}$ 1/s. Solid lines: off-fault unweakened reference lithosphere. Dashed lines: initially weakened lithosphere to localize deformation. The spatial extent of the initially weakened lithosphere is shown in (a) by the three boxes in the ASPECT domain.

bottom to 1615 K. Varying the depth of the lower model boundary (80 km and 110 km instead of 100 km) showed no major influence on modeling results.

2.2.3 Boundary Conditions

The ASPECT model setup is periodic along-strike, which means that the opposing model boundaries in the x-direction are continuously connected in terms of all model variables like velocity, temperature, pressure, and composition. Hence, material can flow out through one boundary and in through the other without leaving the model domain. This allows for a more self-consistent localization of the strike-slip faults since their width and fault-scale kinematics do not need to be prescribed, but can evolve according to the stress field and strain accumulation. Far-field deformation is driven through a prescribed tangential horizontal velocity on the lateral, strike-parallel model sides. The bottom side of the model is governed by free slip boundary conditions and the top is controlled by the equations describing surface processes through coupling with the FastScape code as described in Sec. 2.1. The simulations are run for 20 Myr model time with geodynamic (ASPECT) computational time step sizes of 100,000 years. Each of these time steps includes 10 FastScape time steps of 10,000 years to account for the different time-scales of geodynamic and surface processes. Testing smaller time step sizes showed no impact on modeling results. We use a value of 5 mm/yr for the total boundary velocity in the x-direction, which is in the range of the proposed strike-slip rates for the DSF in the Dead Sea area of 3.8–7 mm/yr (*Le Beon et al.*, 2008; *Hamiel and Piatibratova*, 2019, 2021). In the model setup, the total boundary velocity is divided in half such that the two fault-parallel boundaries are each prescribed a velocity of 2.5 mm/yr in opposite directions. During 20 Myr, this results in a total displacement of 100 km in the models comparable to the accumulated displacement of 105–107 km at the DSF (*Garfunkel*, 1981; *Joffe and Garfunkel*, 1987; *Götze et al.*, 2007; *Mohsen et al.*, 2011).

2.2.4 Rheology

Geodynamic deformation occurs through a visco-plastic rheology including pressure-, temperature- and strain rate-dependent flow laws for viscous diffusion and dislocation creep and Drucker-Prager plasticity for brittle faulting. The evolution of fault systems is furthermore influenced by frictional strain softening over the plastic strain interval of 0–1 (Figure 2b), linearly reducing the internal angle of friction from 30° to 7.5° for strained material, which mimics small-scale processes like chemical alteration of fault gauge, pore pressure changes due to fluid flow along faults, and grain size reduction in frictional shear zones. We introduced initial random noise in the plastic strain field to account for inherited heterogeneity within the geologic units (*Richter et al.*, 2021). By varying the seed value of this noise pattern, we can isolate the impact of early-stage fault localization processes on overall model evolution. Varying the initial noise does not affect our conclusions (Supplementary Material, Figure S1).

To better visualize deformation and fault offsets, we included two initially horizontal layers of 111,042 passive particles at an initial depth of 8 and10 km. By plotting their locations through the evolution of the model, we use them as deformation markers.

2.2.5 Fault Localization

Localization of faults occurs in a self-consistent way. However, the location of major strike-slip faults is introduced by thinning the initial lithospheric mantle layer by 20% (Figure 2c) along three linear segments parallel to the prescribed boundary velocity (Figure 2a). Due to the periodicity of the model, the three segments effectively form two 300 km long fault segments of the evolving transform fault that link in a restraining bend at x = 150 km and a releasing bend at x = 450 km. The compositional perturbation of the lithospheric mantle has a Gaussian shape in the y-direction (east-west) with $\sigma = 5$ km. Thinning the lithosphere alters its internal density and strength distribution. Computing initial isostatic balance leads to initial topographic lows at the surface (Figure 2a). At depth, higher temperatures form a weaker zone that facilitates fault localization. In this way, no initial fault geometries need to be prescribed but all faults form self-consistently according to the prevailing stress field. We have varied the amplitude of the perturbation by a factor of 2 and 0.5, which slightly affects the timing of localization, but this choice does not affect the conclusions. Furthermore, it should be noted that faults in our models do not occur as distinct planes but are represented by a concentration of high strain rates in planar areas with a thickness of a few cells.

The initial strike-perpendicular offset of the segments amounts to 20 km (Figure 2a). During the model run, this leads to a border fault spacing of approximately 10 km at the releasing bend, which corresponds well with observations made at the DSB. Note that increasing or decreasing the offset too much prevents the generation of pull-apart basins. In the fault-parallel direction there is no underlap nor overlap in the prescribed perturbations to maintain the generic character of the models. For transform linkage in extensional settings, previous work (*Neuharth et al.*, 2021) showed no influence of this parameter on the primary model results, given that fault tips consistently propagate in the direction of strike.

2.2.6 Parameter Testing

In this work, we present 11 models. Besides the reference model, we assess the impact of different seeds of the plastic strain initial random noise (1, 3, 5) and different prescribed total boundary velocities in x-direction (2.5 mm/yr, 4.5 mm/yr, 5 mm/yr, 5.5 mm/yr, 10 mm/yr) to investigate the importance of the localization phase (Supplementary Material, Figures S1 and S2).

In terms of surface processes, we present results for four different values of the river incision rate K_f ($1 \cdot 10^{-5}$, $0.5 \cdot 10^{-5}$, $0.25 \cdot 10^{-5}$, $1 \cdot 10^{-40}$ $m^{0.2}$/yr). The first three values represent high, medium, and low surface process efficiency (*Wolf et al.*, 2021) and are within the range of K_f values computed for rivers with varying lithology and climate (*Stock and Montgomery*, 1999). The hillslope diffusion coefficient is kept constant at a value of $1 \cdot 10^{-2}$ $m^{0.2}$/yr, except for the fourth model, where, together with K_f, it was set to a very small value ($1 \cdot 10^{-40}$ $m^{0.2}$/yr). These low values make surface processes very inefficient such that the fourth model evolves according to geodynamic processes only.

Our reference model uses a river incision rate K_f of $0.5 \cdot 10^{-5}$ $m^{0.2}$/yr. When assuming drainage areas of 1 to 15 km^2, this value of K_f is equivalent to the erodibility that has been used for simulating erosion in the Lebanese mountains in previous work (*Goren et al.*, 2015).

2.2.7 Limitations

To derive results that are generally applicable to the dynamics of restraining and releasing bends, but comparable to the DSF area, we decided to employ hybrid models. The first-order geologic setting hence corresponds to the DSF area, while second-order features are deliberately left out to keep a generic character of the setup. We therefore did not include the variations in crustal and lithosphere thicknesses observed in our focus area (*Götze et al.*, 2007; *Mohsen et al.*, 2011; *Smit et al.*, 2008) nor melting, magmatism, grain size evolution, salt tectonics, and potential changes in velocity and thermal boundary conditions (*Garfunkel*, 1981; *Joffe and Garfunkel*, 1987; *Sobolev et al.*, 2005; *Smit et al.*, 2010; *Reilinger and McClusky*, 2011; *Petrunin et al.*, 2012; *Reznik and Bartov*, 2021). Furthermore, the models lack elastic deformation

and evolve under a visco-plastic rheology only. At the along-strike model sides, we use periodic boundary conditions which allow for self-consistent strain localization close to the initial crustal perturbation instead of prescribing fault geometries. Therefore, the initial fault offsets at both bends need to be of the same size, which results in a border fault spacing at the restraining bend that is somewhat smaller than for the Lebanese mountains (*Gomez et al.*, 2007; *Nemer and Meghraoui*, 2020; *Dembo et al.*, 2021) as the perturbations' placing is configured to mimic the size of the Dead Sea. Nevertheless, our simulations capture the first-order structure of the focus region. More importantly, the simplified models allow us to derive robust conclusions concerning the key differences between the evolution of restraining and releasing bends, the interaction between surface processes and tectonics, and the emergence of strain partitioning and local extension in an area where regional tectonics are dominated by strike-slip motion.

3 Results

3.1 Model Evolution

In this section, we describe the evolution of our reference model (Figure 3, also see animation at zenodo.org/doi/10.5281/zenodo.10405076 with explanations in the Supplementary Material). We find that the fault network evolution can be divided into four phases:

3.1.1 Phase I - Localization Determines Deformation Geometry

Deformation in the model is distributed until the main faults localize at ∼2 Myr model time (Figure 3e). At the releasing bend, the two transform segments connect through a straight and narrow deformation zone (Figure 3e, q, u). Contrary to this, the fault tips at the restraining bend maintain an east-west distance of ∼25 km accommodating diffuse deformation (Figure 3e, i, m). Hence, a significant difference exists between the ratios and dimensions of the geologic structures at the two main stepovers. These differences develop even though the initial weakening, length, and spacing of the fault at the left- and right-lateral stepovers are identical.

3.1.2 Phase II - Strong Vertical Motion

In the basin area, phase II starts at ∼5 Myr through the formation of an isolated crustal block that exhibits rapid subsidence (Figure 3f, r). This process coincides with the strain rate induced connection of the brittle parts of the lower crust and lithospheric mantle (Figure 3v). Basin floor subsidence continues until the end of the simulation with a rate of ∼0.6 mm/yr and creates accommodation space for ∼10 km of sediments.

At the surface, a morphology similar to an asymmetric rift appears. Geologic units are horizontal alongside the steep and highly active western fault, while simultaneously, the surface along the eastern fault is bent towards the topographic depression (Figure 3a–b, u–v).

The two faults bounding the mountainous area at the restraining bend develop horse-tail splays that then connect through a strike-slip fault, crosscutting the high elevations. This fault competes with the border faults and gradually takes up more strike-slip deformation, while the earlier faults begin to show reverse faulting components (Figure 3j–l, n–p). The resulting strain partitioning remains until the end of the simulation.

Time-wise, the formation of the new central fault is closely followed by the reaching of the absolute maximum mountain height. Afterwards, elevations decrease since the fault trace becomes smoother and straighter, which reduces compressive stresses and crustal shortening. Note however, that there is vertical movement at the restraining bend at all times (Figure 3j–l, v_v), but after phase II uplift is exceeded by erosion.

3.1.3 Phase III - Fault System Reorganization

The third phase constitutes a gradual transition from phase II to phase IV and is exemplary shown at 15 Myr in Figure 3. While in phase II strike-slip displacement at the restraining bend is distributed over several faults (Figure 3j), it becomes increasingly concentrated on the central fault later on (Figure 3k–l, n–p). This intensifies strain partitioning as the outer faults increasingly deform in a reverse faulting regime. Simultaneously, the viscous domain between the brittle parts of the upper and lower crust gradually vanishes. Eventually, a downward propagation of the central fault connects the brittle crustal layers through an interplay of lower crustal advection and strain rate driven changes in upper crustal rheological behavior (Figure 3o–p).

In the mean time, at the releasing bend, several secondary faults form at the southern and northern ends of the basin. The strike-slip motion is partitioned between those faults, although the main displacement remains focused along the central fault (Figure 3s, v_{II}). The basin floor subsequently splits into several blocks that form terraced basin sidewalls and subbasins with differential sediment accumulation.

3.1.4 Phase IV - Central Faults Dominate the Long-term Fault Network

By the end of the model run at 20 Myr, the main strike-slip displacement is concentrated on the central faults for both stepovers.

In the mountains, the outer faults mainly act in a reverse faulting regime (Figure 3l, p; TF regime) and the fault system undergoes simplification compared to phase II (Figure 3f, n vs. Figure 3h, p). Contrarily, in

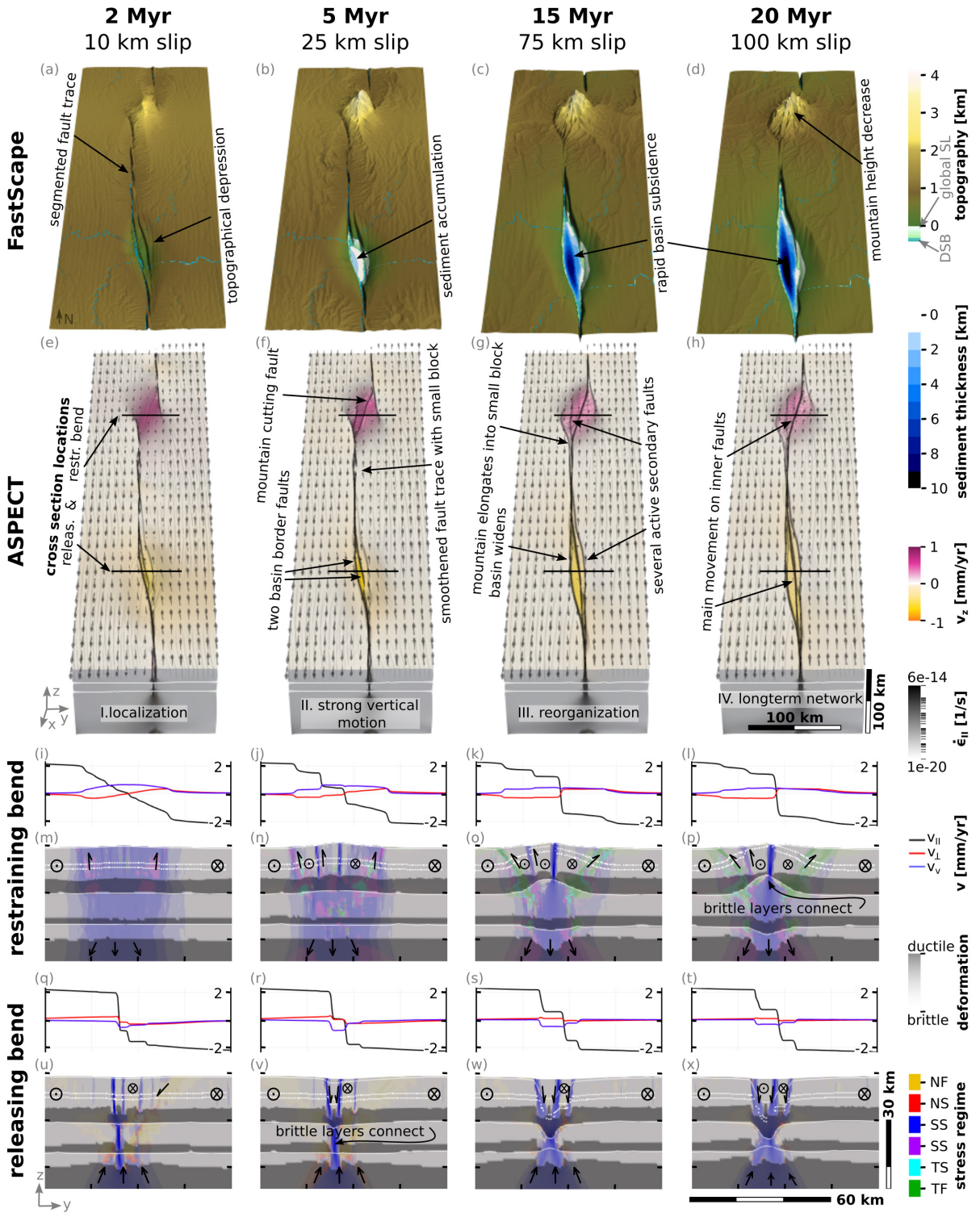

Figure 3 – The four evolutionary phases of the reference model. **(a–d)** FastScape topography and the sediment thickness in marine areas and rivers. Note the difference between the global sea level (global SL) and the local Dead Sea reference lake level (DSB) as indicated in the legend and explained in Sec. 2.1. Model topography is shown relative to global sea level at 0 m. **(e–h)** 3D view of the geodynamic model shows uplift in pink and subsidence in yellow, both overlain by strain rate in black. Arrows represent the magnitude and direction of ASPECT surface velocities. The outlines of the crustal layers are shown in white. **(m–p)** and **(u–x)** show cross sections with the stress regime and deformation regime at the initial stepovers. The initial stepover locations are marked in (e–h). The stress regime categories are based on the World Stress Map project following *Zoback* (1992): NF normal faulting regime, NS transtensional, blue SS strike-slip with less oblique strain axes and therefore unambiguous orientation of the maximum horizontal stress, purple SS strike-slip with more oblique strain axes, TS transpressional, TF thrust faulting. Strong intensities of the stress regime colors coincide with regions of high strain rate. Light areas behave in a brittle manner, while ductile deformation prevails in darker areas. Arrows depict the direction of relative motion of the different blocks, analogous to geological cross sections. The white dotted lines show the current location of the initially horizontal layer of particles at initially 8 and 10 km depth. **(i–l)** and **(q–t)** depict the surface velocity components at the cross sections with black being fault-parallel motion v_{II}, red fault-perpendicular motion $v_{\perp}$, and blue the vertical motion v_v. See the Supplementary Material for a full animation of the reference model.

the basin the fault network becomes more complex during model evolution (Figure 3f, v vs. Figure 3h, x). The outer faults show elements of normal and strike-slip faulting, but accommodate minor displacement compared to the central fault (Figure 3t, x).

To examine the fault network's long-term stability, the simulation was prolonged to 40 Myr. The results indicate that the network established during phase IV at 20 Myr remains stable.

3.2 Comparison to the Dead Sea Area

3.2.1 The Model Reproduces First-order Evolution of the Dead Sea Fault and Basin

The DSF is thought to have formed over 3–4 Myr, likely between 18–14 Ma (*Marco*, 2007; *Oren et al.*, 2020). Similarly, fault localization in the model postdates the onset of strike-slip movement by ∼2 Myr (phase I in Figure 3). As in the model, the topographic depression around the Dead Sea presumably formed prior to the pull-apart basin and is wider than the spacing of the main border faults (*Garfunkel and Ben-Avraham*, 1996), which surround the thickest part of the sedimentary succession (*ten Brink and Ben-Avraham*, 1989; *Garfunkel and Ben-Avraham*, 1996; *Ben-Avraham et al.*, 2008). Basin subsidence is reported to have started at ∼16–15 Ma (*Garfunkel and Ben-Avraham*, 1996; *Calvo and Bartov*, 2001) (seen at 5 Myr model time, phase II in Figure 3) and was enabled by the formation of an isolated crustal block (*Ben-Avraham and Schubert*, 2006) similar to what we see in our models. The sedimentary record shows that the oldest sediments in the DSB came from the E–SE (Jordan/Saudi-Arabia), indicating that the elevated shoulders of the present-day DSB morphology formed later, presumably around 6–5 Ma when basin subsidence accelerated as well (*Garfunkel*, 1981; *Calvo and Bartov*, 2001; *Zilberman and Calvo*, 2013). Today's sediment flux into the DSB derives from various sources. Sediments are transported along-strike by the rivers of the Jordan and Arava valleys, but the main part comes with rivers and creeks from the Jordanian and Judea shoulders of the DSB (*Steinitz and Bartov*, 1992). Similarly, our model shows several sediment sources with material from along-strike directions constituting only ∼30% of the sediment input.

3.2.2 The Model Captures First-order Present-day Structure and Kinematics of the Dead Sea Fault System

Strike-slip motion at the Lebanese restraining bend is concentrated on the central Yammouneh and adjacent faults, while reverse faulting is reported for faults outlining the mountain area (e.g. *Gomez et al.*, 2007; *Elias et al.*, 2007; *Nemer and Meghraoui*, 2020). This results in the same regional strain partitioning between strike-slip and reverse faults that we see in our model results (Figure 3l, p), and that was also observed at other restraining bends (e.g. Jamaica; *Wiggins-Grandison and Atakan*, 2005; *Mann et al.*, 2007).

The main fault pattern along the Dead Sea consists of two subparallel strike-slip to transtensional border faults along an elongated central block (e.g. *Gomez et al.*, 2007; *Elias et al.*, 2007; *Smit et al.*, 2008; *Nemer and Meghraoui*, 2020) (Figure 4a).

In the model results, broad-scale normal faulting is only present in evolutionary phases I and II (Figure 3e–f, u-v) before the second basin bordering fault has localized and strike-slip motion prevails. This two-stage evolution is similar to what has been proposed for the releasing stepover at Lake Kinneret (*Gasperini et al.*, 2020) (Figure 4a). The observed predominantly strike-slip motion along today's DSB (*Hamiel and Piatibratova*, 2019) is hence reproduced by our models. GPS measurements from the Dead Sea area further show local fault-perpendicular motion on the order of 10% of the full strike-slip velocity in the vicinity of the border faults (*Le Beon et al.*, 2008; *Hamiel et al.*, 2009). Similarly, in our models, the fault-perpendicular velocity $v_{\perp}$ component in Figure 3t amounts to ∼5% and the vertical velocity v_v to ∼15% of the prescribed fault-parallel velocity v_{II} of 5 mm/yr. These local displacements cause basin floor subsidence and result from the misalignment of the NNW-SSE-trending main fault trace with the N-S-trending far-field stresses.

Observed seismicity reaches 30 km depth with a maximum at 20–22 km beneath most of the DSB (*Aldersons et al.*, 2003). In our simulations, this depth corresponds to a peak in the energy dissipation rate that occurs within the connected brittle parts of the lower crust and lithospheric mantle (Supplementary Material Figure S4). The energy dissipation rate in model areas with brittle deformation can be used as the equivalent for seismic energy release, and therefore provide information on earthquakes over long time spans in geodynamic models (*Petrunin et al.*, 2012).

3.2.3 Predicted Topography and Structure Match the Dead Sea Basin

Prominent topographical features of the DSB are the asymmetric slopes and the rift-like morphology (*Quennell*, 1959; *Garfunkel*, 1981; *Ben-Avraham and Zoback*, 1992; *DESERT Group et al.*, 2004).

Observed topography and model topography generally agree well (Figure 4a–b, d), especially around the releasing bend (blue lines in Figure 4d). Our reference model does not only closely fit the width, height, and slopes of the basin bounding topography, but also matches the observed maximum sediment thickness of 8–12 km (compare blue lines and blue shaded area in Figure 4d) (*Ten Brink et al.*, 1993; *Garfunkel and Ben-Avraham*,

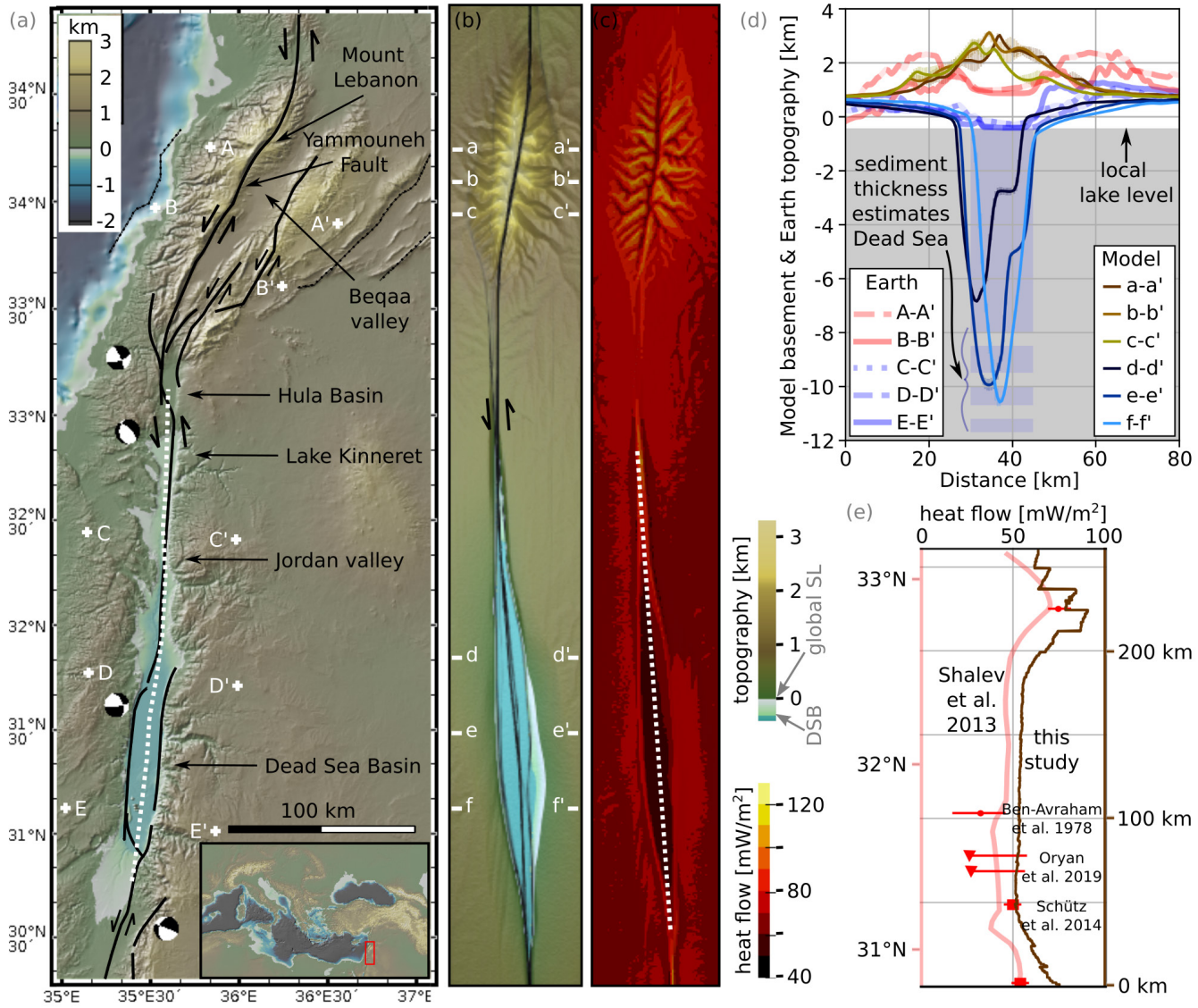

Figure 4 – Comparison of the reference model results to observations from the Dead Sea Fault. **(a)** Present day topography for the DSF area (geomapapp.org, *Ryan et al.*, 2009). Main fault traces (*Styron*, 2019; *Hamiel and Piatibratova*, 2021) with an indication of the direction of motion are shown in black. Dotted black lines mark secondary faults (*Elias et al.*, 2007). Earthquake focal mechanisms are taken from GeoMapApp (*Ekström et al.*, 2012). White letters indicate the profiles plotted in (d), the white dotted line shows the location of the heat flow profile in (e). **(b)** Topography of the reference model after 20 Myr shown on the same scale and with the same color coding as in (a). Logarithmic strain rate is overlain in black and arrows depict the direction of fault motion. White letters indicate the model profiles plotted in (d). **(c)** Modeled surface heat flow after 20 Myr. The white dotted line outlines the modelled heat flow profile in (e). **(d)** Profiles of model topography (lower-case letters and stronger colors) in direct comparison to topography profiles of the Dead Sea area (upper-case letters and transparent lines). The exact locations are shown in (a) and (b). The grey background marks the elevation of the local lake level. Its overlap with model topography profiles gives an estimate of model sediment thickness. The transparent blue rectangle shows the range of published sediment thicknesses for the Dead Sea (8–12 km) (*Götze et al.*, 2007; *Mohsen et al.*, 2011) for comparison. **(e)** Model surface heat flow and published surface heat flow profile for the DSB (*Shalev et al.*, 2013). The locations of the profiles are shown as white dotted lines in (a) and (c). Values in red are surface heat flow measurements with uncertainty and correction ranges taken within the DSB: points (*Ben-Avraham et al.*, 1978), triangles (*Oryan et al.*, 2019), squares (*Schütz et al.*, 2014). Their exact locations are shown in Figure 1b.

1996; *Götze et al.*, 2007; *Mohsen et al.*, 2011). Comparable to the actual DSB (*Garfunkel and Ben-Avraham*, 1996; *Ben-Avraham and Schubert*, 2006), the modeled pull-apart basin is divided into several subbasins. Additionally, our model results show asymmetry in the basin's basement topography (Figure 4d) that is similar to the rift-like morphology of the DSB (*Wdowinski and Zilberman*, 1996; *Lubberts and Ben-Avraham*, 2002) (Figure 1b).

3.2.4 Present-day Surface Heat Flow Trends Agree Between Predictions and Observations

Surface heat flow values of 27–40 mW/m^2 have been reported for the DSB (*Ben-Avraham et al.*, 1978; *Shalev et al.*, 2013; *Schütz et al.*, 2014; *Oryan et al.*, 2019; *Oryan and Savage*, 2021), which is unusually low for an active plate boundary. The low surface heat flow aligns with observations of deep

seismicity which is equally hinting at a brittle and comparably cold lower crust (*Aldersons et al.*, 2003). However, taking accurate measurements of surface heat flow in the DSB environment is challenging (*Oryan et al.*, 2019), for example because they are affected by hydrothermal circulation. Observational uncertainties range between $\pm$2.5 and 14 mW/m^2, or possibly even more (*Schütz et al.*, 2014; *Oryan et al.*, 2019; *Oryan and Savage*, 2021).

In agreement with observations (*Shalev et al.*, 2013), surface heat flow in the modeled pull-apart basin (Figure 4c) is considerably lower than the $\sim$60 mW/m^2 seen in the surrounding, undeformed, areas. This low surface heat flow area is closely confined by the basin bordering faults and thereby constrained to areas with a thick sediment cover. This distribution illustrates the major impact of fast sedimentation rates (e.g., *van Wijk et al.*, 2019), which outpace conductive equilibration of basin temperatures and radioactive heat production. While the absolute values of the modeled surface heat flow are always higher than the observation-based curve, their spatial variations along the center of the pull-apart basin (Figure 4e) show many similarities, e.g., in how they follow the subbasin-structure in both cases (*Shalev et al.*, 2013). The fit of absolute values increases when considering the uncertainty range of available data points (shown in red in Figure 4e), and the remaining differences may be attributed to the partly generic character of our models.

South of 33°N, observations suggest a distinct peak in surface heat flow at Lake Kinneret (Figure 4e) that is similarly seen in our model results. In both observations and predictions, this surface heat flow signal is tightly bounded by faults. However, while the signal at Lake Kinneret is underlain by a small stepover, within our simulations the high surface heat flow occurs at a transform fault segment. Previous studies have proposed that the high values are related to a crustal heat source from a paleo-thermal event at 5.3–3.5 Ma (*Heimann et al.*, 1996; *Reznik and Bartov*, 2021). Our models, however, can alternatively explain this feature via a dominant role of shear heating through strike-slip tectonics.

According to our simulations, surface heat flow at the restraining bend is expected to be locally variable, with values in the valleys reaching up to 120 mW/m^2 and lower values of 60–70 mW/m^2 on the ridges. When considering the entire mountain range, the average surface heat flow is 80–90 mW/m^2. The high variability can be explained by the above-average erosion rate in the valleys leading to rock exhumation from greater depths. In the absence of heat flow measurements at the Lebanon mountains, our reference model provides a first-order approximation of the surface heat flow and its pattern in that region.

3.3 Interaction Between Surface Processes and Tectonics

We isolate the influence of surface processes by varying the efficiency of the stream power law (Supplementary Material, eq. 9) through the river incision rate, K_f, while all other parameters of the reference model remain unchanged except for the model with minimal surface process efficiency where the hill slope diffusion is reduced as well (Figure 5). For increased surface process efficiency (through an increased K_f), mountain heights decrease and the volume of the sediment infill within the pull-apart basin increases. This supports previous work on sediment infill of basins without drainage (*Berry et al.*, 2019). At the restraining bend, topography and strain partitioning patterns show gradual changes connected to the value of K_f. At the releasing bend, however, we find a stark contrast between models with minimal surface process efficiency and those with higher degrees of erosion. This contrast is expressed in first-order changes to the basin shape and topography (Figure 5q vs. Figure 5r–t). The availability of sediments triggers a threshold behavior for pull-apart basin evolution that we describe in the following paragraph.

3.3.1 Sediments Control Longevity of Pull-apart Basin

In the simulation with minimal surface processes efficiency, the maximum basement depth never exceeds 4 km below sea level. In the presence of sediments, this value increases to $\sim$10 km (Figure 5r, s, t), clearly showing how sediments create their own accommodation space (e.g., *Bond and Kominz*, 1988; *Mahattanachai et al.*, 2021; *Neuharth et al.*, 2022a) by inducing basement subsidence in this spatially restricted continental setting. By filling the basin, the sediments load the hanging walls of steeply dipping strike-slip faults and thereby induce a flexural fault rotation towards shallower dip angles (Figure 5q–t). This process enhances the misalignment of the NNW-SSE-trending Dead Sea Fault with the N-S-trending far-field stresses, which leads to more pronounced local extension (Sec. 3.2) that is not related to far-field divergence. In the models including sedimentation, the pull-apart basins do not stop evolving but new main faults continuously form towards the center. In the model with minimal surface processes efficiency, i.e. without sedimentation (Figure 5q), on the contrary, basin evolution stops around 15 Myr and strike-slip faults do not renew nor change geometry. At the surface they are in close vicinity and tend to dip away from the basin.

3.3.2 Erosion Increases Strain Partitioning

At the restraining bend, mountain heights vary between 2 km for high surface process efficiency (K_f=$1 \cdot 10^{-5}$ m$^{0.2}$/yr) and $>$ 6 km with minimal surface processes (K_f=$1 \cdot 10^{-40}$ m$^{0.2}$/yr) (Figure 5a–d).

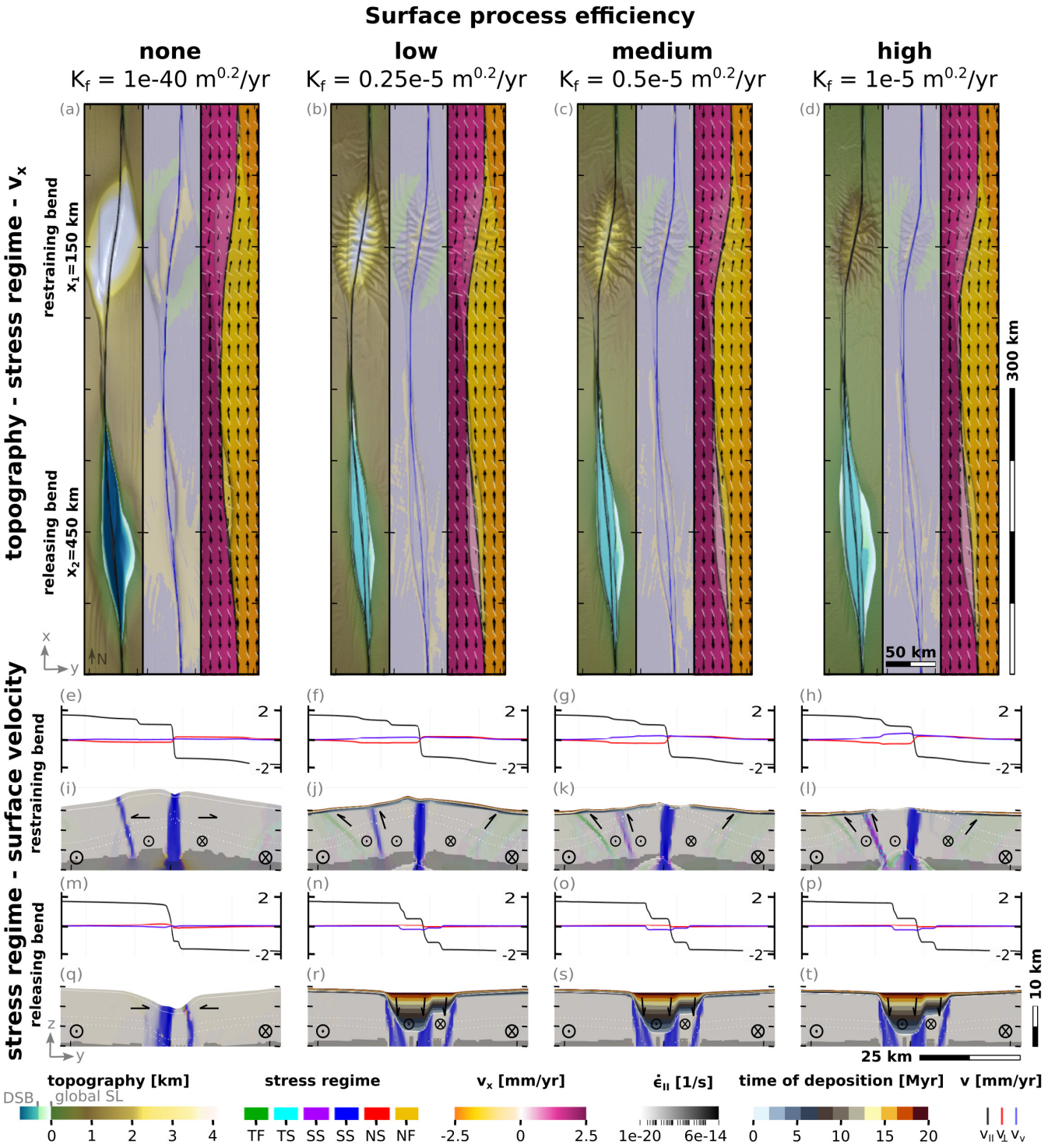

Figure 5 – **(a–d)** Surface topography, stress regime and surface velocities (from left to right) at 20 Myr model time for four different surface process efficiencies. Our reference model is shown in panels c,g,k,o,s. Note the difference between the global sea level (global SL) and the local Dead Sea reference lake level (DSB) as indicated in the legend. Topography and velocity are overlain by the logarithmic strain rate in black shades. The stress regime categories are based on the World Stress Map project following *Zoback* (1992): NF normal faulting regime, NS transtensional, blue SS strike-slip with less oblique strain axes and therefore unambiguous orientation of the maximum horizontal stress, purple SS strike-slip with more oblique strain axes, TS transpressional, TF thrust faulting. Black arrows in the surface velocity plots show magnitude and direction of the full velocity while the x-component of velocity is shown in pink to yellow colors. **(i–l)** and **(q-t)** show cross sections of the stress regime at the locations of the initial stepovers with the restraining bend at x_1 = 150 km and the releasing bend at x_2 = 450 km as shown in (a–d). Strong intensities of the stress regime colors coincide with regions of high strain rate. Light areas behave in a brittle manner, while ductile deformation prevails in darker areas. Arrows depict relative motions of the different blocks analog to geological cross sections. The white dotted lines show the current location of the initially horizontal layer of particles used as deformation markers. **(e-h)** and **(m-p)** depict the surface velocity components along the cross sections, with black being fault-parallel motion v_{II}, red fault-perpendicular motion $v_{\perp}$, and blue the vertical motion v_v.

Elevations hence vary substantially with K_f, while spatial variations and changes in the surface outline of the fault network are minor. However, the along-strike surface velocity reveals that the number of strike-slip faults decreases with increasing K_f (see the steps in the black lines of Figure 5e–h). This is in agreement with previous studies that found decreasing fault network complexity but increasing fault longevity caused by surface processes (*Olive et al.*, 2014; *Neuharth et al.*, 2022b).

The unloading of the hanging wall at strike-slip faults with a thrust component leads to faster exhumation (*Willett*, 1999). The tectonic stress regime in Figure 5e–l therefore shows a positive correlation between K_f and the amount of reverse faulting and associated uplift below the mountains (see $v_\perp$ and v_v). Such a connection has been hypothesized for the uplift at the Jamaican restraining bend (*Cochran et al.*, 2017) and for the amount of topographic elevation of restraining bends in general (*Cowgill et al.*, 2004) and is corroborated by our models.

3.3.3 Surface Processes Affect Crustal Deformation Patterns

Crustal deformation patterns depend on the stepover orientation, with crustal thinning occurring around the releasing bend and thickening around the restraining bend. Both processes are enhanced by increased efficiency of surface processes (Figure 6 and Supplementary Table S3). In the following, we quantify their impact by comparing the reference model (Figure 5c) to the model with minimal surface processes (Figure 5a). At the restraining bend, 39% of thickening occurs due to tectonic processes, while erosion balances this value with ∼15% of thinning to a total crustal thickening of ∼24%. The basement beneath the pull-apart basin experiences 23% of thinning in the simulation without surface processes, with an additional ∼18% of thinning related to sedimentation. The crust in the reference model's releasing bend therefore experiences a total thinning of 41%. However, due to diffuse off-fault deformation (*Herbert et al.*, 2014), crustal deformation is not confined to the pull-apart and mountain area, both in nature and models. We identify a crustal deformation pattern that resembles coupled non-channelized crustal flow (*Royden*, 1996) with horizontal velocities continuously increasing towards the surface for the entire lithosphere. Crustal flow described for many orogens is driven by gravitational potential energy and moves crustal material away from thickened crust and high elevations (e.g. *Royden et al.*, 1997). A similar flow is thickening the crust adjacent to the restraining bend in our models (Figure 6).

Notably, we isolate a second direction of material flow which is seemingly opposed to gravitational potential energy. This flow component is generated by the sediment infill of the pull-apart basin which generates crustal motions that are directed away from the basin. This type of sedimentation-driven return flow has been previously described in highly sedimented rifted margins surrounding South-East Asian orogens (*Morley and Westaway*, 2006; *Clift*, 2015). The speed of return flow was shown to anti-correlate with crustal viscosity (*Clift et al.*, 2015). Due to the relatively high strength of our model crust, this velocity component has only a maximum speed of 0.02 mm/yr. Nevertheless, we find that it enhances vertical movement at the restraining bend.

4 Discussion

A key controversy surrounding the DSB is whether or not far-field extension played a role in its creation. On one hand, plate kinematic studies inferred a change in Sinai's Euler pole ∼5 Ma (*Garfunkel*, 1981; *Joffe and Garfunkel*, 1987; *Reilinger and McClusky*, 2011), which added a small component of transverse extension at the southern sector of the DSF and a component of transverse contraction at the northern, Lebanese sector of the DSF. The timing corresponds to uplift of the shoulders of the DSB (*Chaldekas et al.*, 2021) and has also been used to explain the rift-like morphology of the basin (*Quennell*, 1959; *Garfunkel*, 1981; *Ben-Avraham and Zoback*, 1992). On the other hand, regional GPS observations do not support a present-day component of far-field divergence across the fault (*Le Beon et al.*, 2008; *Hamiel and Piatibratova*, 2021). Our model shows that the velocity field near the releasing bend rotates, which creates a local component of east-west extension that varies between 5 and 10% of the relative plate motion (Figure 3q-t) during the 20 Myr of model evolution. This effect is further enhanced by sedimentation (Sec. 3.3). To explicitly investigate the effect of far-field extension, we added 0.5 mm/yr of east-west divergence to our boundary conditions (i.e., 10% of the relative plate motion) during the last 5 Myr of the simulation. This results in a total extension of 2.5 km, a value used in previous studies of the DSF (*Sobolev et al.*, 2005, and references therein). These boundary conditions result in a basin that is wider and longer than in the reference model (Supplementary Figure S3). In addition, the restraining bend shows no reverse faulting and far too little elevation ($<$1 km). Because these model characteristics do not fit observations of the DSB, while the reference model without an extensional component does, we conclude that the asymmetric rift morphology of the DSB can form under pure strike-slip conditions. This finding is in agreement with previous 3D geodynamic models of the DSB (*Petrunin et al.*, 2012) as well as with analog models of generic releasing bends (*Smit et al.*, 2008) and the paired bend of the Marmara Sea and Ganos mountains (*Bulkan et al.*, 2020). Our model basins, however, lack uplifted shoulders (blue lines in Figure 4d) that have been linked to compression near the fault tips (*van Wijk et al.*, 2017), a process that is present in our models. We attribute this discrepancy either to elastic processes that are known to alter

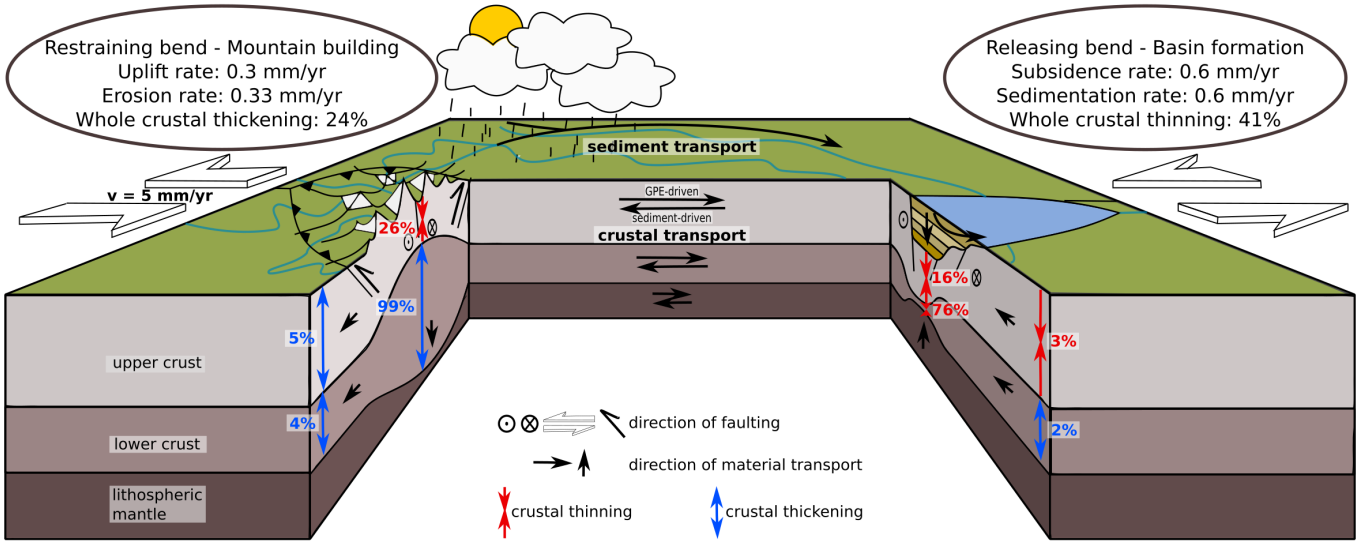

Figure 6 – A summary sketch of the model results depicting the material transport between the releasing and restraining stepover with black arrows. The pattern of crustal thinning and thickening is visualized with red and blue arrows, respectively. The length of the arrows is not to scale. The values for velocities and changes in crustal thickness are computed from the reference model at 20 Myr. At the releasing bend, higher surface process efficiency increases basin growth and crustal thinning. At the restraining bend, crustal thickening is counteracted by erosion, which thins the upper crust. Except in this part of the model domain, crustal thinning and thickening effects generally intensify with increasing surface process efficiency. Model sediments are transported from the higher elevations at and around the restraining bend towards the releasing bend where they induce continued basin growth and subsidence. Basin growth in turn fuels crustal transport towards the restraining bend, where it enhances uplift rates and strain partitioning. This flow is opposed to the GPE-driven flow away from thickened crust. For models with different surface process efficiencies, the changes in crustal thickness over 20 Myr are summarized in the Supplementary Material in Table S3.

topography (*Olive et al.*, 2016) or to events in the thermal evolution (*Petrunin et al.*, 2012), both of which we do not include.

We further find that sedimentation prolongs tectonic activity of the pull-apart basin. Sediment loading creates a pressure that drives isostatic subsidence and balances horizontal gravitational potential energy gradients. This leads to both bordering faults remaining active (*Zwaan et al.*, 2018) and facilitates local extension (*Neuharth et al.*, 2022a). This finding changes the view on the longevity of pull-apart basins. While some studies suggested that the lifetime and growth of both narrow and wider pull-apart basins are limited by the development of a basin crossing fault (*Wu et al.*, 2009; *Sugan*, 2014; *van Wijk et al.*, 2017), we see no sign of ceasing growth when running our setup to 40 Myr. Instead, continued sedimentation enables the basin to grow in length and depth while active faults are continuously being replaced by pairs of younger, more central faults. This leads to the formation of elongated terraces (e.g., *Dooley and McClay*, 1997; *Wu et al.*, 2009) and a subbasin structure. Continuous fault replacement was hypothesised by previous studies using prescribed faults (*van Wijk et al.*, 2017) and can now be confirmed by our models due to their ability to spontaneously form faults during the model evolution. Conversely, the evolution of the pull-apart basin in our model without surface processes stagnates at ~15 Myr. We therefore conclude that the increasing sediment load plays a major role for the longevity of pull-apart basins, which has previously mainly been linked to the basin geometry (*van Wijk et al.*, 2017). Notably, only 30% of the model sediment infill arrives along-strike from the restraining bend, while the remaining 70% are derived from the areas bordering the basin. This makes our results also applicable to pull-apart basins without a restraining bend nearby.

Considering that the geometry of the initial crustal perturbations inducing the restraining and releasing bend is the same, we find a striking difference between the shapes of the pull-apart basin and the push-up mountain. The mountain fault system outline is ellipsoidal with a length-to-width ratio of ~2, while this ratio for the basin border faults is ~8 (Figure 3h). The shape results from the favorable orientation of the local stress field. The NNW-SSE oriented strike-slip faults that accommodate the left-lateral stepover at the releasing bend coincide with the overall NNW-SSE directed maximum horizontal stress (Figure 5), and therefore localize during the first phase of model evolution. The SSW-NNE directed faults of the restraining bend are, however, less favorably oriented so that it takes more time for a segment-connecting fault to develop. Examples for these characteristic shapes can be found in natural paired bends like the DSF system (*Smit et al.*, 2008; *Nemer and Meghraoui*, 2020), but also at the Hendrix pull-apart basin with the Jamaican restraining bend (*Mann et al.*, 2007).

5 Conclusions

Despite their partly generic nature, our 3D models of a restraining and a releasing bend match a multitude of observables from the Dead Sea Fault System. The asymmetric basement and the unusually thick sediment infill of the DSB have been linked to a variety of processes. We show that both features can emerge under purely strike-slip boundary conditions and are a direct consequence of the localization processes. We further find that the very deep and narrow basin is a result of sediment loading within the basin. Observed surface heat flow values for the DSB area are $\sim$50 mW/m^2 and show a specific pattern along the fault that is reproduced by our simulations. In the Lebanon Mountains, where observational heat flow data is sparse, the models predict higher surface heat flow.

In a more general way, our models demonstrate how erosion and sedimentation are key factors for the longevity and size of pull-apart basins in an active tectonic environment. Furthermore, we quantify the impact of surface processes on the crustal thinning and thickening pattern seen at the releasing and the restraining bend, respectively (Figure 6). The model results reveal that the two fault bends are linked by along-strike material transport at a crustal level, which intensifies with surface process efficiency. This transport is driven by gravitational potential energy in conjunction with sediment deposition. At the restraining bend, this manifests as enhanced strain partitioning because of continued and accelerated vertical movement.

Acknowledgements

The work was supported by the North-German Supercomputing Alliance (HLRN). We gratefully acknowledge the computing time granted by the Resource Allocation Board and provided on the supercomputer Lise and Emmy at NHR@ZIB and NHR@Göttingen as part of the NHR infrastructure. The calculations for this research were conducted with computing resources under the project bbp00064. We thank the Computational Infrastructure for Geodynamics (geodynamics.org) which is funded by the National Science Foundation under award EAR-0949446 and EAR-1550901 for supporting the development of ASPECT. ELH is grateful for financial support from the Geo.X Young Academy. SB has been funded by the European Union (ERC, EMERGE, 101087245). SVS was supported by a grant from the European Research Council (ERC, Synergy Grant MEET, 856555). We furthermore thank J. C. Duarte, A. Balasz and anonymous reviewers for their constructive feedback.

Author contributions

Modeling, writing and visualization was mainly conducted by **ELH** in close cooperation with **SB** and **ACG** and guidance by **SVS**. Software development and model setup has been performed by **ELH** and **DN**. Regional geology of the DSF was contributed by **RG** and **YH**.

Data availability

The ASPECT and FastScape software versions used in this paper as well as the used input files (*Heckenbach*, 2023) are available at zenodo.org/doi/10.5281/zenodo.10405076.

Competing interests

The authors declare no competing interests.

Peer review

This publication was peer-reviewed by Attila Balazs and Joao Duarte. The full peer-review report can be found here: tektonika.online/index.php/home/article/view/75/98

Copyright notice

References

Aldersons, F., Z. Ben-Avraham, A. Hofstetter, E. Kissling, and T. Al-Yazjeen (2003), Lower-crustal strength under the Dead Sea basin from local earthquake data and rheological modeling, *Earth and Planetary Science Letters*, *214*(1), 129–142, doi: 10.1016/S0012-821X(03)00381-9.

Arpat, E. (1972), The East Anatolian fault system: thoughts on its development, *MTA Bull.*, *78*, 33–39.

Ben-Avraham, Z., and G. Schubert (2006), Deep "drop down" basin in the southern Dead Sea, *Earth and Planetary Science Letters*, *251*(3), 254–263, doi: 10.1016/j.epsl.2006.09.008.

Ben-Avraham, Z., and M. D. Zoback (1992), Transform-normal extension and asymmetric basins: An alternative to pull-apart models, *Geology*, *20*(5), 423–426, doi: 10.1130/0091-7613(1992)020<0423:TNEAAB>2.3.CO;2.

Ben-Avraham, Z., R. Hänel, and H. Villinger (1978), Heat flow through the Dead Sea rift, *Marine Geology*, *28*(3), 253–269, doi: 10.1016/0025-3227(78)90021-X.

Ben-Avraham, Z., Z. Garfunkel, and M. Lazar (2008), Geology and Evolution of the Southern Dead Sea Fault with Emphasis on Subsurface Structure, *Annual Review of Earth and Planetary Sciences*, *36*(1), 357–387, doi: 10.1146/annurev.earth.36.031207.124201.

Ben-Avraham, Z., V. Lyakhovsky, and G. Schubert (2010), Drop-down formation of deep basins along the Dead Sea and other strike-slip fault systems, *Geophysical Journal International*, *181*(1), 185–197, doi: 10.1111/j.1365-246X.2010.04525.x.

Berry, M., J. van Wijk, D. Cadol, E. Emry, and D. Garcia-Castellanos (2019), Endorheic-Exorheic Transitions of the Rio Grande and East African Rifts, *Geochemistry, Geophysics, Geosystems*, *20*(7), 3705–3729, doi: 10.1029/2018GC008176.

Bond, G. C., and M. A. Kominz (1988), Evolution of thought on passive continental margins from the origin of geosynclinal theory (∼1860) to the present, *GSA Bulletin*, *100*(12), 1909–1933, doi: 10.1130/0016-7606(1988)100<1909:EOTOPC>2.3.CO;2.

Braun, J., and S. D. Willett (2013), A very efficient O(n), implicit and parallel method to solve the stream power equation governing fluvial incision and landscape evolution, *Geomorphology*, *180-181*, 170–179, doi: 10.1016/j.geomorph.2012.10.008.

Bulkan, S., P. Henry, P. Vannucchi, F. Storti, C. Cavozzi, and J. P. Morgan (2020), The evolution of restraining and releasing bend pairs: analogue modelling investigation and application to the Sea of Marmara, *preprint*, Geology, doi: 10.1002/essoar.10502140.1.

Calvo, R., and J. Bartov (2001), Hazeva Group, southern Israel: New observations, and their implications for its stratigraphy, paleogeography, and tectono-sedimentary regime., *Isr. J. Earth Sci.*, *50*(2-4), 71–99.

Chaldekas, O., A. Vaks, I. Haviv, A. Gerdes, and R. Albert (2021), U-Pb speleothem geochronology reveals a major 6 Ma uplift phase along the western margin of Dead Sea Transform, *GSA Bulletin*, *134*(5-6), 1571–1584, doi: 10.1130/B36051.1.

Clift, P. D. (2015), Coupled onshore erosion and offshore sediment loading as causes of lower crust flow on the margins of South China Sea, *Geoscience Letters*, *2*(1), 13, doi: 10.1186/s40562-015-0029-9.

Clift, P. D., S. Brune, and J. Quinteros (2015), Climate changes control offshore crustal structure at South China Sea continental margin, *Earth and Planetary Science Letters*, *420*, 66–72, doi: 10.1016/j.epsl.2015.03.032.

Cochran, W. J., J. A. Spotila, P. S. Prince, and R. J. McAleer (2017), Rapid exhumation of Cretaceous arc-rocks along the Blue Mountains restraining bend of the Enriquillo-Plantain Garden fault, Jamaica, using thermochronometry from multiple closure systems, *Tectonophysics*, *721*, 292–309, doi: 10.1016/j.tecto.2017.09.021.

Cowgill, E., A. Yin, J. R. Arrowsmith, W. X. Feng, and Z. Shuanhong (2004), The Akato Tagh bend along the Altyn Tagh fault, northwest Tibet 1: Smoothing by vertical-axis rotation and the effect of topographic stresses on bend-flanking faults, *GSA Bulletin*, *116*(11-12), 1423–1442, doi: 10.1130/B25359.1.

Crowell, J. C. (1974), Origin of Late Cenozoic Basins in Southern California (Abstract-AAPG Bulletin, 1973, p. 774; article-SEPM Special Publication No. 22, 194, p. 190-204), *Tectonics and Sedimention*, pp. 190–204.

Dembo, N., R. Granot, and Y. Hamiel (2021), Mechanical contrast and asymmetric distribution of crustal deformation across plate boundaries: Insights from the northern Dead Sea fault system, *Geology*, *49*(5), 498–503, doi: 10.1130/G48342.1.

DESERT Group, M. Weber, K. Abu-Ayyash, A. Abueladas, A. Agnon, H. Al-Amoush, A. Babeyko, Y. Bartov, M. Baumann, Z. Ben-Avraham, G. Bock, J. Bribach, R. El-Kelani, A. Förster, H.-J. Förster, U. Frieslander, Z. Garfunkel, S. Grunewald, H. J. Götze, V. Haak, C. Haberland, M. Hassouneh, S. Helwig, A. Hofstetter, K.-H. Jäckel, D. Kesten, R. Kind, N. Maercklin, J. Mechie, A. Mohsen, F. M. Neubauer, R. Oberhänsli, I. Qabbani, O. Ritter, G. Rümpker, M. Rybakov, T. Ryberg, F. Scherbaum, J. Schmidt, A. Schulze, S. Sobolev, M. Stiller, H. Thoss, U. Weckmann, and K. Wylegalla (2004), The crustal structure of the Dead Sea Transform, *Geophysical Journal International*, *156*(3), 655–681, doi: 10.1111/j.1365-246X.2004.02143.x.

Dooley, T., and K. McClay (1997), Analog Modeling of Pull-Apart Basins, *AAPG Bulletin*, *81*(11), 1804–1826, doi: 10.1306/3B05C636-172A-11D7-8645000102C1865D.

Dubertret, L. (1932), Les formes structurales de la Syrie et de la Palestine, *Comptes Rendus de l'Académie des Sciences*, *195*, 66–68.

Ekström, G., M. Nettles, and A. M. Dziewonski (2012), The global CMT project 2004-2010: Centroid-moment tensors for 13,017 earthquakes, *Phys. Earth Planet. Inter.*, pp. 1–9, doi: 10.1016/j.pepi.2012.04.002.

Elias, A., P. Tapponnier, S. C. Singh, G. C. King, A. Briais, M. Daëron, H. Carton, A. Sursock, E. Jacques, R. Jomaa, and Y. Klinger (2007), Active thrusting offshore Mount Lebanon: Source of the tsunamigenic A.D. 551 Beirut-Tripoli earthquake, *Geology*, *35*(8), 755–758, doi: 10.1130/G23631A.1.

Fedorik, J., F. E. Maesano, and A. M. Afifi (2022), A validated geomechanical model for the strike-slip restraining bend in lebanon, *Scientific Reports*, *12*(1), 20,071, doi: 10.1038/s41598-022-24718-0.

Fraters, M. R. T., W. Bangerth, C. Thieulot, A. C. Glerum, and W. Spakman (2019), Efficient and practical Newton solvers for non-linear Stokes systems in geodynamic problems, *Geophysical Journal International*, *218*(2), 873–894, doi: 10.1093/gji/ggz183.

Förster, H. J., A. Förster, R. Oberhänsli, and D. Stromeyer (2010), Lithospheric composition and thermal structure of the Arabian Shield in Jordan, *Tectonophysics*, *481*(1), 29–37, doi: 10.1016/j.tecto.2008.11.014.

Garfunkel, Z. (1981), Internal structure of the Dead Sea leaky transform (rift) in relation to plate kinematics, *Tectonophysics*, *80*(1), 81–108, doi: 10.1016/0040-1951(81)90143-8.

Garfunkel, Z., and Z. Ben-Avraham (1996), The structure of the Dead Sea basin, *Tectonophysics*, *266*(1), 155–176, doi: 10.1016/S0040-1951(96)00188-6.

Garfunkel, Z., and Z. Ben-Avraham (2001), Basins along the Dead Sea Transform, *Basins along the Dead Sea Transform*, *186*, 607–627.

Gasperini, L., M. Lazar, A. Mazzini, M. Lupi, A. Haddad, C. Hensen, M. Schmidt, A. Caracausi, M. Ligi, and A. Polonia (2020), Neotectonics of the Sea of Galilee (northeast Israel): implication for geodynamics and seismicity along the Dead Sea Fault system, *Scientific Reports*, *10*(1), 11,932, doi: 10.1038/s41598-020-67930-6.

Gassmöller, R., H. Lokavarapu, E. Heien, E. G. Puckett, and W. Bangerth (2018), Flexible and Scalable Particle-in-Cell Methods With Adaptive Mesh Refinement for Geodynamic Computations, *Geochemistry, Geophysics, Geosystems*, *19*(9), 3596–3604, doi:

10.1029/2018GC007508.

Gilbert, G. K., R. Humphrey, J. Sewell, and F. Soule (1907), The earthquake as a natural phenomenon, *The San Francisco Earthquake and Fire, US Geol. Surv. Bull*, *324*, 1–13.

Glerum, A., C. Thieulot, M. Fraters, C. Blom, and W. Spakman (2018), Nonlinear viscoplasticity in ASPECT: benchmarking and applications to subduction, *Solid Earth*, *9*(2), 267–294, doi: 10.5194/se-9-267-2018.

Gomez, F., T. Nemer, C. Tabet, M. Khawlie, M. Meghraoui, and M. Barazangi (2007), Strain partitioning of active transpression within the Lebanese restraining bend of the Dead Sea Fault (Lebanon and SW Syria), *Geological Society, London, Special Publications*, *290*(1), 285–303, doi: 10.1144/290.10.

Goren, L., S. Castelltort, and Y. Klinger (2015), Modes and rates of horizontal deformation from rotated river basins: Application to the Dead Sea fault system in Lebanon, *Geology*, *43*(9), 843–846, doi: 10.1130/G36841.1.

Götze, H.-J., R. El-Kelani, S. Schmidt, M. Rybakov, M. Hassouneh, H.-J. Förster, and J. Ebbing (2007), Integrated 3D density modelling and segmentation of the Dead Sea Transform, *International Journal of Earth Sciences*, *96*(2), 289–302, doi: 10.1007/s00531-006-0095-5.

Hamiel, Y., and O. Piatibratova (2019), Style and Distribution of Slip at the Margin of a Pull-Apart Structure: Geodetic Investigation of the Southern Dead Sea Basin, *Journal of Geophysical Research: Solid Earth*, *124*(11), 12,023–12,033, doi: 10.1029/2019JB018456.

Hamiel, Y., and O. Piatibratova (2021), Spatial Variations of Slip and Creep Rates Along the Southern and Central Dead Sea Fault and the Carmel–Gilboa Fault System, *Journal of Geophysical Research: Solid Earth*, *126*(9), e2020JB021,585, doi: 10.1029/2020JB021585.

Hamiel, Y., R. Amit, Z. B. Begin, S. Marco, O. Katz, A. Salamon, E. Zilberman, and N. Porat (2009), The Seismicity along the Dead Sea Fault during the Last 60,000 Years, *Bulletin of the Seismological Society of America*, *99*(3), 2020–2026, doi: 10.1785/0120080218.

Heckenbach, E. (2023), Strike slip modeling - Dead-Sea: Heckenbach et al, doi: 10.5281/zenodo.10405077.

Heimann, A., G. Steinitz, D. Mor, and G. Shaliv (1996), The Cover Basalt Formation, its age and its regional and tectonic setting: Implications from K-Ar and 40Ar/39Ar geochronology, *Isr. J. Earth Sci*, *45*(5).

Heister, T., J. Dannberg, R. Gassmöller, and W. Bangerth (2017), High Accuracy Mantle Convection Simulation through Modern Numerical Methods. II: Realistic Models and Problems, *Geophysical Journal International*, *210*(2), 833–851, doi: 10.1093/gji/ggx195.

Herbert, J. W., M. L. Cooke, M. Oskin, and O. Difo (2014), How much can off-fault deformation contribute to the slip rate discrepancy within the eastern California shear zone?, *Geology*, *42*(1), 71–75, doi: 10.1130/G34738.1.

Joffe, S., and Z. Garfunkel (1987), Plate kinematics of the circum Red Sea—a re-evaluation, *Tectonophysics*, *141*(1), 5–22, doi: 10.1016/0040-1951(87)90171-5.

Ketin, I. (1948), Über die tektonisch-mechanischen folgerungen aus den grossen anatolischen erdbeben des letzten dezenniums, *Geologische Rundschau*, *36*(1), 77–83.

Kronbichler, M., T. Heister, and W. Bangerth (2012), High Accuracy Mantle Convection Simulation through Modern Numerical Methods, *Geophysical Journal International*, *191*, 12–29, doi: 10.1111/j.1365-246X.2012.05609.x.

Lateef, A. S. A. (2007), Geological history of the bekaa valley, in *Second International Conference on the Geology of the Tethys*, pp. 391–402.

Lawson, A. C. (1895), *Sketch of the geology of the San Francisco Peninsula*, US Government Printing Office.

Le Beon, M., Y. Klinger, A. Q. Amrat, A. Agnon, L. Dorbath, G. Baer, J.-C. Ruegg, O. Charade, and O. Mayyas (2008), Slip rate and locking depth from GPS profiles across the southern Dead Sea Transform, *Journal of Geophysical Research: Solid Earth*, *113*(B11), doi: 10.1029/2007JB005280.

Lubberts, R. K., and Z. Ben-Avraham (2002), Tectonic evolution of the Qumran Basin from high-resolution 3.5-kHz seismic profiles and its implication for the evolution of the northern Dead Sea Basin, *Tectonophysics*, *346*(1), 91–113, doi: 10.1016/S0040-1951(01)00230-X.

Mahattanachai, T., C. K. Morley, P. Charusiri, and P. Kanjanapayont (2021), The Andaman Basin Central Fault Zone, Andaman Sea: Characteristics of a major deepwater strike-slip fault system in a polyphase rift, *Marine and Petroleum Geology*, *128*, 104,997, doi: 10.1016/j.marpetgeo.2021.104997.

Mann, P. (2007), Global catalogue, classification and tectonic origins of restraining- and releasing bends on active and ancient strike-slip fault systems, *Geological Society, London, Special Publications*, *290*, 13–142, doi: 10.1144/SP290.2.

Mann, P., C. Demets, and M. Wiggins-Grandison (2007), Toward a better understanding of the Late Neogene strike-slip restraining bend in Jamaica: geodetic, geological, and seismic constraints, *Geological Society, London, Special Publications*, *290*(1), 239–253, doi: 10.1144/SP290.8.

Marco, S. (2007), Temporal variation in the geometry of a strike–slip fault zone: Examples from the Dead Sea Transform, *Tectonophysics*, *445*(3), 186–199, doi: 10.1016/j.tecto.2007.08.014.

Mohsen, A., G. Asch, J. Mechie, R. Kind, R. Hofstetter, M. Weber, M. Stiller, and K. Abu-Ayyash (2011), Crustal structure of the Dead Sea Basin (DSB) from a receiver function analysis, *Geophysical Journal International*, *184*(1), 463–476, doi: 10.1111/j.1365-246X.2010.04853.x.

Morley, C. K., and R. Westaway (2006), Subsidence in the super-deep Pattani and Malay basins of Southeast Asia: a coupled model incorporating lower-crustal flow in response to post-rift sediment loading, *Basin Research*, *18*(1), 51–84, doi: 10.1111/j.1365-2117.2006.00285.x.

Nemer, T. S., and M. Meghraoui (2020), A non-active fault within an active restraining bend: The case of the Hasbaya fault, Lebanon, *Journal of Structural Geology*, *136*, 104,060, doi: 10.1016/j.jsg.2020.104060.

Neuharth, D., S. Brune, A. Glerum, C. Heine, and J. K. Welford (2021), Formation of Continental Microplates Through Rift Linkage: Numerical Modeling and Its Application to the Flemish Cap and Sao Paulo Plateau, *Geochemistry, Geophysics, Geosystems*, *22*(4), e2020GC009,615, doi: 10.1029/2020GC009615.

Neuharth, D., S. Brune, A. Glerum, C. K. Morley, X. Yuan, and J. Braun (2022a), Flexural strike-slip basins, *Geology*, *50*(3), 361–365, doi: 10.1130/G49351.1.

Neuharth, D., S. Brune, T. Wrona, A. Glerum, J. Braun, and X. Yuan (2022b), Evolution of Rift Systems and Their Fault Networks in Response to Surface Processes, *Tectonics*, *41*(3), e2021TC007,166, doi: 10.1029/2021TC007166.

Norris, R. J., and V. G. Toy (2014), Continental transforms: A view from the Alpine Fault, *Journal of Structural Geology*, *64*, 3–31, doi: 10.1016/j.jsg.2014.03.003.

Olive, J.-A., M. D. Behn, and L. C. Malatesta (2014), Modes of extensional faulting controlled by surface processes, *Geophysical Research Letters*, *41*(19), 6725–6733, doi: 10.1002/2014GL061507.

Olive, J.-A., M. D. Behn, E. Mittelstaedt, G. Ito, and B. Z. Klein (2016), The role of elasticity in simulating long-term tectonic extension, *Geophysical Journal International*, *205*(2), 728–743, doi: 10.1093/gji/ggw044.

Oren, O., P. Nuriel, A. R. C. Kylander-Clark, and I. Haviv (2020), Evolution and Propagation of an Active Plate Boundary: U-Pb Ages of Fault-Related Calcite From the Dead Sea Transform, *Tectonics*, *39*(8), e2019TC005,888, doi: 10.1029/2019TC005888.

Oryan, B., and H. Savage (2021), Regional Heat Flow Analysis Reveals Frictionally Weak Dead Sea Fault, *Geochemistry, Geophysics, Geosystems*, *22*(12), e2021GC010,115, doi: 10.1029/2021GC010115.

Oryan, B., H. Villinger, M. Lazar, M. J. Schwab, I. Neugebauer, and Z. Ben-Avraham (2019), Heat flow in the Dead Sea from the ICDP boreholes and its implication for the structure of the basin, *Quaternary Science Reviews*, *210*, 103–112, doi: 10.1016/j.quascirev.2019.02.016.

Petrunin, A., and S. V. Sobolev (2006), What controls thickness of sediments and lithospheric deformation at a pull-apart basin?, *Geology*, *34*(5), 389, doi: 10.1130/G22158.1.

Petrunin, A. G., E. Meneses Rioseco, S. V. Sobolev, and M. Weber (2012), Thermomechanical model reconciles contradictory geophysical observations at the Dead Sea Basin, *Geochemistry, Geophysics, Geosystems*, *13*(4), doi: 10.1029/2011GC003929.

Quennell, A. M. (1959), Tectonics of the dead sea rift, in *Proceedings of the 20th international geological congress, Mexico*, pp. 385–403.

Rayleigh, L. (1916), Lix. on convection currents in a horizontal layer of fluid, when the higher temperature is on the under side, *The London, Edinburgh, and Dublin Philosophical Magazine and Journal of Science*, *32*(192), 529–546.

Reilinger, R., and S. McClusky (2011), Nubia-Arabia-Eurasia plate motions and the dynamics of Mediterranean and Middle East tectonics: Mediterranean and Middle East geodynamics, *Geophysical Journal International*, *186*(3), 971–979, doi: 10.1111/j.1365-246X.2011.05133.x.

Reznik, I. J., and Y. Bartov (2021), Present Heat Flow and Paleo-Geothermal Anomalies in the Southern Golan Heights, Israel, *Earth and Space Science*, *8*(3), e2020EA001,299, doi: 10.1029/2020EA001299.

Richter, M. J. E. A., S. Brune, S. Riedl, A. Glerum, D. Neuharth, and M. R. Strecker (2021), Controls on Asymmetric Rift Dynamics: Numerical Modeling of Strain Localization and Fault Evolution in the Kenya Rift, *Tectonics*, *40*(5), e2020TC006,553, doi: 10.1029/2020TC006553.

Rose, I., B. Buffett, and T. Heister (2017), Stability and accuracy of free surface time integration in viscous flows, *Physics of the Earth and Planetary Interiors*, *262*, 90 – 100, doi: 10.1016/j.pepi.2016.11.007.

Royden, L. (1996), Coupling and decoupling of crust and mantle in convergent orogens: Implications for strain partitioning in the crust, *Journal of Geophysical Research: Solid Earth*, *101*(B8), 17,679–17,705, doi: 10.1029/96JB00951.

Royden, L. H., B. C. Burchfiel, R. W. King, E. Wang, Z. Chen, F. Shen, and Y. Liu (1997), Surface Deformation and Lower Crustal Flow in Eastern Tibet, *Science*, *276*(5313), 788–790, doi: 10.1126/science.276.5313.788.

Ryan, W. B. F., S. M. Carbotte, J. O. Coplan, S. O'Hara, A. Melkonian, R. Arko, R. A. Weissel, V. Ferrini, A. Goodwillie, F. Nitsche, J. Bonczkowski, and R. Zemsky (2009), Global Multi-Resolution Topography synthesis, *Geochemistry, Geophysics, Geosystems*, *10*(3), doi: 10.1029/2008GC002332.

Schütz, F., H. J. Förster, and A. Förster (2014), Thermal conditions of the central Sinai Microplate inferred from new surface heat-flow values and continuous borehole temperature logging in central and southern Israel, *Journal of Geodynamics*, *76*, 8–24, doi: 10.1016/j.jog.2014.02.010.

Seymen, İ., and A. Aydin (2023), The bingöl earthquake fault and its relation to the north anatolian fault zone, *Bulletin of the Mineral Research and Exploration*, *1972*(79), 1.

Shalev, E., V. Lyakhovsky, Y. Weinstein, and Z. Ben-Avraham (2013), The thermal structure of Israel and the Dead Sea Fault, *Tectonophysics*, *602*, 69–77, doi: 10.1016/j.tecto.2012.09.011.

Smit, J., J.-P. Brun, S. Cloetingh, and Z. Ben-Avraham (2008), Pull-apart basin formation and development in narrow transform zones with application to the Dead Sea Basin, *Tectonics*, *27*(6), doi: 10.1029/2007TC002119.

Smit, J., J. P. Brun, S. Cloetingh, and Z. Ben-Avraham (2010), The rift-like structure and asymmetry of the Dead Sea Fault, *Earth and Planetary Science Letters*, *290*(1), 74–82, doi: 10.1016/j.epsl.2009.11.060.

Sobolev, S., A. Petrunin, Z. Garfunkel, and A. Babeyko (2005), Thermo-mechanical model of the Dead Sea Transform, *Earth and Planetary Science Letters*, *238*(1-2), 78–95, doi: 10.1016/j.epsl.2005.06.058.

Steinitz, G., and Y. Bartov (1992), The Miocene-Pleistocene history of the Dead Sea segment of the Rift in light of K-Ar ages of basalts, *Israel Journal of Earth-Sciences*, *38*(2-4), 199–208.

Stock, J. D., and D. R. Montgomery (1999), Geologic constraints on bedrock river incision using the stream power law, *Journal of Geophysical Research: Solid Earth*, *104*(B3), 4983–4993, doi: 10.1029/98JB02139.

Styron, R. (2019), GEMScienceTools/gem-global-active-faults: First release of 2019, doi: 10.5281/zenodo.3376300.

Sugan, M. (2014), 3D Analogue Modelling of Transtensional Pull-apart Basins: comparison with the Cinarcik Basin, Sea of Marmara, Turkey, *BGTA*, doi: 10.4430/bgta0129.

Tapponnier, P., and P. Molnar (1977), Active faulting and tectonics in China, *Journal of Geophysical Research*, *82*(20), 2905–2930, doi: 10.1029/JB082i020p02905.

ten Brink, U. S., and Z. Ben-Avraham (1989), The anatomy of a pull-apart basin: Seismic reflection observations of the Dead Sea Basin, *Tectonics*, *8*(2), 333–350, doi: 10.1029/TC008i002p00333.

Ten Brink, U. S., Z. Ben-Avraham, R. E. Bell, M. Hassouneh, D. F. Coleman, G. Andreasen, G. Tibor, and B. Coakley (1993), Structure of the Dead Sea pull-apart basin from

gravity analyses, *Journal of Geophysical Research: Solid Earth*, *98*(B12), 21,877–21,894, doi: 10.1029/93JB02025.

van Wijk, J., G. Axen, and R. Abera (2017), Initiation, evolution and extinction of pull-apart basins: Implications for opening of the Gulf of California, *Tectonophysics*, *719-720*, 37–50, doi: 10.1016/j.tecto.2017.04.019.

van Wijk, J. W., S. P. Heyman, G. J. Axen, and P. Persaud (2019), Nature of the crust in the northern Gulf of California and Salton Trough, *Geosphere*, *15*(5), 1598–1616, doi: 10.1130/GES02082.1.

van Zelst, I., F. Crameri, A. E. Pusok, A. Glerum, J. Dannberg, and C. Thieulot (2022), 101 geodynamic modelling: how to design, interpret, and communicate numerical studies of the solid Earth, *Solid Earth*, *13*(3), 583–637, doi: 10.5194/se-13-583-2022.

Wdowinski, S., and E. Zilberman (1996), Kinematic modelling of large-scale structural asymmetry across the Dead Sea Rift, *Tectonophysics*, *266*(1), 187–201, doi: 10.1016/S0040-1951(96)00238-7.

Wellman, H. (1952), The Alpine Fault in detail: river terrace displacement at Maruia River, *New Zealand Journal of Science and Technology B*, *33*, 409–414.

Wetzler, N., and I. Kurzon (2016), The Earthquake Activity of Israel: Revisiting 30 Years of Local and Regional Seismic Records along the Dead Sea Transform, *Seismological Research Letters*, *87*(1), 47–58, doi: 10.1785/0220150157.

Wiggins-Grandison, M. D., and K. Atakan (2005), Seismotectonics of Jamaica, *Geophysical Journal International*, *160*(2), 573–580, doi: 10.1111/j.1365-246X.2004.02471.x.

Willett, S. D. (1999), Orogeny and orography: The effects of erosion on the structure of mountain belts, *Journal of Geophysical Research: Solid Earth*, *104*(B12), 28,957–28,981, doi: 10.1029/1999JB900248.

Wolf, S. G., R. S. Huismans, J.-A. Muñoz, M. E. Curry, and P. van der Beek (2021), Growth of Collisional Orogens From Small and Cold to Large and Hot—Inferences From Geodynamic Models, *Journal of Geophysical Research: Solid Earth*, *126*(2), e2020JB021,168, doi: 10.1029/2020JB021168.

Wu, J. E., K. McClay, P. Whitehouse, and T. Dooley (2009), 4D analogue modelling of transtensional pull-apart basins, *Marine and Petroleum Geology*, *26*(8), 1608–1623, doi: 10.1016/j.marpetgeo.2008.06.007.

Yuan, X. P., J. Braun, L. Guerit, D. Rouby, and G. Cordonnier (2019a), A New Efficient Method to Solve the Stream Power Law Model Taking Into Account Sediment Deposition, *Journal of Geophysical Research: Earth Surface*, *124*(6), 1346–1365, doi: 10.1029/2018JF004867.

Yuan, X. P., J. Braun, L. Guerit, B. Simon, B. Bovy, D. Rouby, C. Robin, and R. Jiao (2019b), Linking continental erosion to marine sediment transport and deposition: A new implicit and O(N) method for inverse analysis, *Earth and Planetary Science Letters*, *524*, 115,728, doi: 10.1016/j.epsl.2019.115728.

Zilberman, E., and R. Calvo (2013), Remnants of Miocene fluvial sediments in the Negev Desert, Israel, and the Jordanian Plateau: Evidence for an extensive subsiding basin in the northwestern margins of the Arabian plate, *Journal of African Earth Sciences*, *82*, 33–53, doi: 10.1016/j.jafrearsci.2013.02.006.

Zoback, M. L. (1992), First- and second-order patterns of stress in the lithosphere: The World Stress Map Project, *Journal of Geophysical Research: Solid Earth*, *97*(B8), 11,703–11,728, doi: 10.1029/92JB00132.

Zwaan, F., G. Schreurs, and J. Adam (2018), Effects of sedimentation on rift segment evolution and rift interaction in orthogonal and oblique extensional settings: Insights from analogue models analysed with 4D X-ray computed tomography and digital volume correlation techniques, *Global and Planetary Change*, *171*, 110–133, doi: 10.1016/j.gloplacha.2017.11.002.